

Optimal design of stand-alone solutions based on RES + hydrogen storage feeding off-grid communities

*Original*

Optimal design of stand-alone solutions based on RES + hydrogen storage feeding off-grid communities / Marocco, Paolo; Ferrero, Domenico; Lanzini, Andrea; Santarelli, Massimo. - In: ENERGY CONVERSION AND MANAGEMENT. - ISSN 0196-8904. - ELETTRONICO. - 238:(2021), p. 114147. [10.1016/j.enconman.2021.114147]

*Availability:*

This version is available at: 11583/2917772 since: 2021-08-13T12:17:58Z

*Publisher:*

Elsevier

*Published*

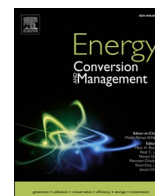
DOI:10.1016/j.enconman.2021.114147

*Terms of use:*

This article is made available under terms and conditions as specified in the corresponding bibliographic description in the repository

*Publisher copyright*

(Article begins on next page)



# Optimal design of stand-alone solutions based on RES + hydrogen storage feeding off-grid communities

Paolo Marocco<sup>\*</sup>, Domenico Ferrero, Andrea Lanzini, Massimo Santarelli

Department of Energy, Politecnico di Torino, Corso Duca degli Abruzzi 24, 10129 Torino, Italy

## ARTICLE INFO

### Keywords:

Hydrogen  
Electrolysis  
Off-grid  
Optimal sizing  
Battery  
Energy storage

## ABSTRACT

Concerning off-grid areas, diesel engines still dominate the scene of local electricity generation, despite the related pollution concerns and high operating costs. There is thus a huge global potential, in remote areas, for exploiting local renewable energy sources (RES) in place of fossil generation. Energy storage systems become hence essential for off-grid communities to cope with the issue of RES intermittency, allowing them to rely on locally harvested RES.

In this work, we analysed different typologies of off-grid renewable power systems, involving batteries and hydrogen as means to store energy, to find out which is the most cost-effective configuration in remote areas. Both Li-ion and lead-acid batteries were included in the analysis, and both alkaline and PEM electrolysis technologies were considered for the production of hydrogen. Starting from single cell electrochemical models, the performance curves of the electrolyser and fuel cell devices were derived for a more detailed techno-economic assessment. Lifetimes of batteries and H<sub>2</sub>-based components were also computed based on how the power-to-power (P2P) system operates along the reference year. The particle swarm optimization (PSO) algorithm was employed to find the component sizes that allow minimizing the levelized cost of energy (LCOE) while keeping the off-grid area energy autonomous. As a case study, the Ginostra village, on the island of Stromboli (North of Sicily, Southern Italy), was analysed since it is well representative of small insular locations in the Mediterranean area. The renewable P2P solution (0.51 €/kWh for the cheapest configuration) was found to be economically preferable than the current existing power system relying on diesel generators (0.86 €/kWh). Hydrogen, in particular, can prevent the oversizing of both battery and PV systems, thus reducing the final cost of electricity delivered by the P2P system. Moreover, unlike diesel generators, the RES-based configuration allows avoiding the production of local air pollutants and GHG emissions during its operation.

## 1. Introduction

Villages in off-grid remote areas mainly rely on the usage of diesel generators [1]. Grid connections, when feasible, are also considered as a possible choice. However, the required infrastructure to make the connection is generally expensive and invasive and the area would often face connection problems (e.g., instability and outages) due to its remoteness [2]. Alternative solutions need therefore to be considered to limit fossil fuels-related problems (e.g., environmental pollution and transportation/logistic issues) and avoid the need for unreliable and costly connections to the grid. There is hence significant potential for incorporating renewable energy sources (RES) into mini-grid systems. When dealing with RES, electrical energy storage (EES) technologies become key system components to make the community energy

autonomous. EES devices allow in fact to match load and supply, thus solving the problem of intermittency of locally harvested RES [3,4].

In this contest, hydrogen can represent an interesting energy storage option given its high energy density, long-term storage capability and cleanness in terms of local pollutants and CO<sub>2</sub> emitted [5]. Increasing attention is therefore focusing on the investigation of hydrogen usage in off-grid remote areas, also analysing its integration with batteries. An H<sub>2</sub>-based energy system is a so-called 'power-to-power' (P2P) solution, which comprises of an electrolyzer to convert the surplus RES energy into hydrogen, a pressurized container for gas storage and a fuel cell for producing electricity back during power shortage. Zhang *et al.* [6], Maleki *et al.* [7] and Nordin *et al.* [8] reported that a power system with batteries only is economically preferable to a configuration relying on hydrogen only, due to the high investment costs and short lifespan of H<sub>2</sub>-based components. The energy storage hybridization (i.e., both battery

<sup>\*</sup> Corresponding author.

E-mail address: [paolo.marocco@polito.it](mailto:paolo.marocco@polito.it) (P. Marocco).

<https://doi.org/10.1016/j.enconman.2021.114147>

Received 16 November 2020; Accepted 6 April 2021

Available online 23 April 2021

0196-8904/© 2021 The Authors.

Published by Elsevier Ltd.

This is an open access article under the CC BY-NC-ND license

(<http://creativecommons.org/licenses/by-nc-nd/4.0/>).

Acronyms			
ABSO	Artificial bee swarm optimization	KPI	Key performance indicator
ACO	Ant colony optimization	LA	Lead-acid
ALK	Alkaline	LCOE	Levelized cost of energy
ASR	Area specific resistance	LHV	Lower heating value
BOP	Balance of plant	LI	Lithium-ion
BT	Battery	LOH	Level of hydrogen
C	Configuration	LPSP	Loss of power supply probability
CSA	Crow search algorithm	LT	Lifetime throughput
CTF	Cycles-to-failure	MBA	Mine blast algorithm
DC	Direct current	NPC	Net present cost
DOD	Depth-of-discharge	NR	No replacement
EES	Electrical energy storage	OM	Operation & maintenance
EL	Electrolyzer	PEM	Proton exchange membrane
EMS	Energy management strategy	P2P	Power-to-power
FC	Fuel cell	PSO	Particle swarm optimization
FPA	Flower pollination algorithm	PV	Photovoltaics
GA	Genetic algorithm	RES	Renewable energy source
GHG	Greenhouse gas	SA	Simulated annealing
HRES	Hybrid renewable energy system	SC	Supercapacitor
HS	Harmony search	SOC	State of charge
HT	Hydrogen tank	TMY	Typical meteorological year

and hydrogen) remains more expensive than the case with only batteries according to Castañeda *et al.* [9] and Hosseinalizadeh *et al.* [10]. However, renewable hydrogen can become a competitive solution in stand-alone power systems since it can help to prevent the oversizing of batteries [2]. Off-grid systems relying on a suitable combination of both batteries and hydrogen are reported to be the most cost-effective solution by Dong *et al.* [11] and Dawood *et al.* [12], who analysed and compared the performance of different combinations of hybrid renewable energy systems (HRES) for remote communities. Similarly, an off-grid hybrid battery/hydrogen system was found to have lower cost than the other analysed configurations by Li *et al.* [13], due to the advantage of both the high efficiency of batteries and the low cost of high capacity hydrogen tanks. Richards *et al.* [14] showed that hydrogen-based technologies become economically viable for HRESs located at more extreme latitudes, where the seasonal variation of the solar radiation is relevant. The economic profitability of a stand-alone battery-hydrogen system was proved by Nordin *et al.* [15] in case the excess renewable energy is converted into hydrogen and then sold to local consumers for the transportation sector. Hydrogen was also found to be profitable by Gracia *et al.* [16] when the seasonality of PV production is relevant, the available surface for PV installation is limited and the electrical load during night is high. A similar consideration was derived by Perrigot *et al.* [17], who observed hydrogen to become more interesting than batteries when high amount of electricity consumption occurs at night. Stand-alone systems based on diesel generators can be more cost-effective [16,18]; however, their economic viability is highly dependent on the cost of fuel [19]. Ashourian *et al.* [18] showed that diesel-based systems become more expensive than the green energy configuration when the diesel fuel price is higher than 2.20 \$/L. It is also noteworthy that, unlike diesel, RES integrated with battery/hydrogen technologies for the development of a self-sustained power system can lead to advantages from an environmental point of view, since GHG emissions are significantly reduced [20]. According to the economic analysis performed by Ozden *et al.* [21], solar-hydrogen based renewable energy systems most likely will become an economically competitive alternative to conventional diesel generators in the near future thanks to the decreasing trend of PV panel costs and the rising diesel fuel prices.

System cost and reliability must be addressed when designing a stand-alone hybrid renewable energy system. Optimal sizing means in

fact to effectively satisfy the load demand at all times while minimizing a certain objective function, e.g., system cost (or cost of energy) in case single-objective optimization is performed. The HOMER software tool is often considered for the optimal sizing of HRESs [22]. Alternatively, metaheuristic optimization algorithms are also commonly employed [23]. Due to its high performance and robustness [7], the particle swarm optimization (PSO) is one of the most used methods when dealing with the optimal design of renewable power systems [24]. Genetic algorithm (GA) technique has also been extensively applied, showing its effectiveness especially when dealing with multi-objective optimization [25,26]. A broader overview about intelligent techniques adopted to optimally design stand-alone H<sub>2</sub>-based systems is shown in Table 1.

In the present study, the optimal sizing of off-grid hydrogen-based energy systems has been investigated. The optimization was performed by means of the PSO technique with the aim of minimizing the levelized cost of energy (LCOE). As shown in Table 1, studies dealing with the design optimization of hydrogen storage systems usually model the electrolyzer and fuel cell devices by assuming a constant efficiency. In this work, detailed electrochemical models provide part-load performance curves of both the electrolyzer and fuel cell to be used within the optimization routine. This is particularly suited when dealing with devices that need to adapt continuously their operating point to match the intermittent power supply from on-site renewable sources. The electrolyzer and fuel cell lifespans were also derived based on the yearly number of simulated working hours and start-ups, for a better assessment of the P2P system costs. Moreover, cost estimation was made more precise by introducing scale dependencies of costs for the H<sub>2</sub> devices. Different energy storage configurations were analysed considering various types of batteries (Li-ion and lead acid) and electrolyzers (alkaline and PEM) to better investigate the role and potential of hydrogen in off-grid environments. The optimal sizing methodology was then applied to assess the most cost-effective storage solution for a real off-grid insular community (southern Italy), which is well representative of many other insular locations across the Mediterranean area. The selected case study is also part of REMOTE [41], project belonging to the EU's Horizon 2020 program.

The structure of this paper is as follows: Section 2 describes the proposed RES-based solution and the models of all the system components along with the adopted control strategy. Section 3 provides the methodology for the optimal sizing of the system together with the

**Table 1**

Literature review about the optimal design of stand-alone hydrogen-based energy systems.

Authors	Year	Algorithm for optimal sizing	Storage configurations	EL and FC performance
Maleki et al. [7]	2014	PSO	BT; H <sub>2</sub>	Const.
Maleki et al. [27]	2014	ABSO	H <sub>2</sub>	Const.
Kalinci et al. [28]	2015	HOMER <sup>a</sup>	H <sub>2</sub>	Const.
Behzadi et al. [29]	2015	GA, HOMER <sup>a</sup>	BT-H <sub>2</sub>	Eff. curve <sup>b</sup>
Baghaee et al. [30]	2016	PSO	H <sub>2</sub>	Const.
Dong et al. [11]	2016	ACO	BT; H <sub>2</sub> ; BT-H <sub>2</sub>	Const.
Fathy [31]	2016	MBA	H <sub>2</sub>	Const.
Ahadi et al. [32]	2017	HOMER <sup>a</sup>	BT; H <sub>2</sub> ; BT-H <sub>2</sub>	Const.
Li et al. [33]	2017	GA	BT-H <sub>2</sub>	Const. <sup>c</sup>
Gracia et al. [16]	2018	ODYSSEY <sup>a</sup>	BT (*2); BT-H <sub>2</sub>	Eff. curve <sup>d</sup>
Duman et al. [34]	2018	HOMER <sup>a</sup>	BT; H <sub>2</sub>	Const.
Zhang et al. [6]	2018	SA	BT; H <sub>2</sub>	Const.
Samy et al. [35]	2019	FPA	H <sub>2</sub>	Const.
Moghaddam et al. [36]	2019	FPA	H <sub>2</sub>	Const.
Jamshidi et al. [19]	2019	CSA	H <sub>2</sub>	Const.
Luta et al. [37]	2019	HOMER <sup>a</sup>	H <sub>2</sub> -SC	Const.
Rullo et al. [38]	2019	GA	BT-H <sub>2</sub>	Const. <sup>c</sup>
Attemene et al. [26]	2020	GA	BT-H <sub>2</sub> -SC	Const.
Dawood et al. [12]	2020	HOMER <sup>a</sup>	BT; H <sub>2</sub> ; BT-H <sub>2</sub>	Const.
Perrigot et al. [17]	2020	PSO	BT-H <sub>2</sub>	Const.
Xu et al. [39]	2020	GA	H <sub>2</sub>	Const.
Zhang et al. [40]	2020	HS	H <sub>2</sub>	Const.
Our work		PSO	BT (*2); H <sub>2</sub> (*2); BT-H <sub>2</sub> (*4)	Eff. curve <sup>e</sup>

<sup>a</sup> Simulation tool.

<sup>b</sup> Linear expression for power and hydrogen consumption curves.

<sup>c</sup> Linearization of the performance curve (MILP-based system operation).

<sup>d</sup> Polynomial efficiency for electrolyzer and constant for fuel cell.

<sup>e</sup> Efficiency curve derived from detailed bottom-up electrochemical models.

evaluation of the objective function to be minimized (i.e., the levelized cost of energy). Section 4 introduces the reference case study presenting its current situation and the necessity for alternatives to the diesel-based solution. In Section 5 main results from the optimal sizing of all the investigated system configurations are presented and discussed. Finally, conclusions are reported in Section 6. In the Appendix, more information about the electrolyzer and fuel cell models are shown, including the adopted model parameters and graphs displaying the various over-voltage contributions.

The overall optimization framework considered in this work is summed up in Fig. 1.

## 2. System modelling

The stand-alone power system under analysis consists of the following components: PV panels, a bank of batteries (BT) and a hydrogen-based storage system, which includes an electrolyzer (EL), a pressurized hydrogen tank (HT) and a fuel cell (FC). The schematic representation of the system is reported in Fig. 2. Since the operating pressure of the electrolyzer is assumed to be equal to the H<sub>2</sub> tank maximum pressure, the compression step between the electrolyzer and the pressurized hydrogen tank is not necessary [2].

### 2.1. PV system

The output of the PV system was evaluated as follows [42]:

$$P_{PV}(t) = f_{PV} \cdot P_{PV, rated} \cdot \frac{G(t)}{G_{STC}} \cdot (1 + \gamma_T \cdot (T_{cell}(t) - T_{cell, STC})) \quad (1)$$

Where  $G$  (in kW/m<sup>2</sup>) is the total irradiance incident on the PV array,  $G_{STC}$  (equal to 1 kW/m<sup>2</sup>) is the incident irradiance at standard test conditions,  $P_{PV, rated}$  (in kW) is the rated PV power,  $T_{cell}$  (in °C) is the PV

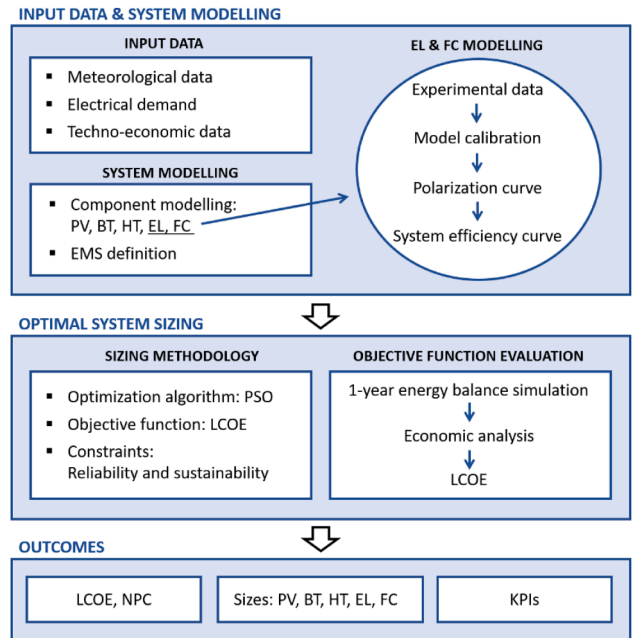


**Fig. 1.** Optimization framework to optimally design the renewable P2P system.

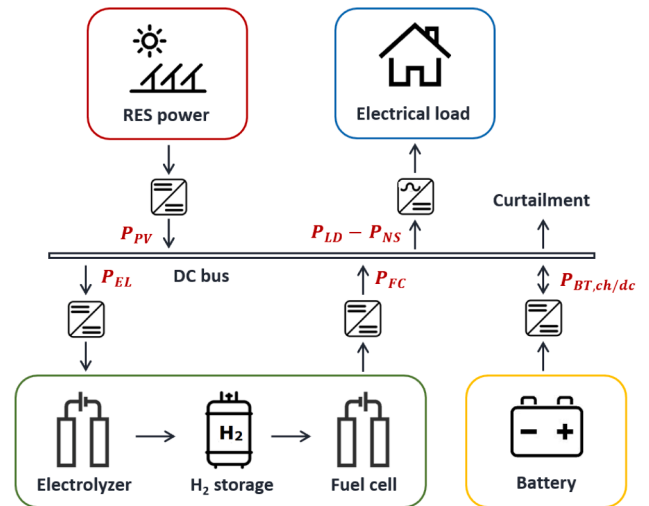


**Fig. 2.** Layout of the renewable P2P system.

cell temperature,  $T_{cell, STC}$  (equal to 25 °C) corresponds to the PV cell temperature at standard test conditions,  $f_{PV}$  is the derating factor and  $\gamma_T$  (in 1/K) is the temperature coefficient.

The cell temperature  $T_{cell}$  was expressed as [43]:

$$T_{cell}(t) = T_a(t) + \frac{G(t)}{0.8} \cdot (NOCT - 20) \quad (2)$$

Where  $T_a$  (in °C) is the ambient temperature and  $NOCT$  (in °C) represents the nominal operating cell temperature.

The total irradiance  $G$  over the tilted PV surface was expressed as [44,45]:

$$G(t) = G_{b,n}(t) \cdot \cos(\theta) + G_{d,h}(t) \cdot F_{c,s} + G_{t,h}(t) \cdot \rho_g \cdot F_{c,g} \quad (3)$$

Where  $G_{b,n}$  (in kW/m<sup>2</sup>) is the direct normal irradiance,  $G_{d,h}$  (in kW/m<sup>2</sup>) is the diffusive irradiance on the horizontal surface,  $G_{t,h}$  (in kW/m<sup>2</sup>) is the total irradiance on the horizontal surface,  $\rho_g$  is the albedo of ground,  $F_{c,s}$  is the collector-sky view factor,  $F_{c,g}$  is the collector-ground view factor and  $\theta$  is the angle of incidence of the beam solar radiation

on the tilted surface.

The hourly values of diffusive and total irradiance on the horizontal plane, direct normal irradiance and ambient temperature were taken from the Photovoltaic geographical information system (PVGIS) software [46], referring to a typical meteorological year (TMY) for the location under analysis.

The albedo of the ground was assumed equal to 0.2. This average value is suggested by Laoun *et al.* [44] when no specific information about the location are available. The terms  $F_{c,s}$  and  $F_{c,g}$ , which depend on the slope of the titled PV surface ( $\beta$ ), were derived according to the relationship reported in [44]. The following equation was finally applied to evaluate the angle of incidence  $\theta$ :

$$\cos(\theta) = \cos(\beta) \cdot \cos(\theta_z) + \sin(\beta) \cdot \sin(\theta_z) \cdot \cos(\phi_s - \phi) \quad (4)$$

Where  $\theta_z$  is the zenith angle,  $\phi_s$  is the solar azimuth and  $\phi$  is the surface azimuth. The zenith angle and the solar azimuth were calculated from [44]. Optimal values for the PV surface slope and surface azimuth were derived from [46].

## 2.2. Electrolyzer and fuel cell

Electrochemical models were formulated for the electrolyzer (alkaline and PEM) and PEM fuel cell devices. This allows for a proper description of their behaviour, which is typically nonlinear. Experimental polarization curves were used to calibrate the models and compute the value of various fitted parameters. More in detail, experimental data from Henao *et al.* [47], Marocco *et al.* [48] and Corrêa *et al.* [49] were considered for the validation of the alkaline electrolyzer, PEM electrolyzer and PEM fuel cell models, respectively. Fitted parameters, whose values were obtained by the calibration process, and fixed parameters of the models are reported in the Appendix. Model calibration was carried out by minimizing the sum of the squares of the difference between experimental and model values of the cell operating voltage.

The operating cell voltage is described by the reversible voltage increased (for the electrolyzer) or decreased (for the fuel cell) by irreversible losses including the activation, ohmic and diffusion contributions:

$$V_{cell} = V_{rev} \pm V_{act} \pm V_{ohm} \pm V_{diff} \quad (5)$$

Where  $V_{rev}$  (in V) stands for the reversible thermodynamic potential and  $V_{act}$ ,  $V_{ohm}$  and  $V_{diff}$  (in V) represent the activation, ohmic and diffusion overpotentials, respectively.

Below, main equations of the electrochemical models are reported.

### 2.2.1. Alkaline electrolyzer

The reversible cell voltage was expressed as [50]:

$$V_{rev} = V_{rev}(T, p_0) + \frac{R_U \cdot T}{2 \cdot F} \ln \left( \frac{(p_{cat} - p_{V,KOH}) \cdot (p_{an} - p_{V,KOH})^{0.5}}{a_{H_2O,KOH}} \right) \quad (6)$$

Where  $F$  corresponds to the Faraday constant (equal to 96,485C/mol),  $T$  (in K) is the operating temperature,  $R_U$  is the universal gas constant (equal to 8.314 J/mol/K),  $p_{an/cat}$  (in bar) is the anode/cathode operating pressure,  $p_{V,KOH}$  (in bar) is the vapor pressure of the KOH solution and  $a_{H_2O,KOH}$  is the water activity of the KOH solution.

The term  $V_{rev}(T, p_0)$ , which corresponds to the reversible voltage as a function of temperature and at reference standard pressure of 1 bar, was computed according to the polynomial expression from [50]. The vapor pressure and the water activity of the KOH solution were defined using the relationships presented in [51].

The activation overpotential at the anode and cathode side was derived from the Butler-Volmer equation:

$$V_{act,an/cat} = \frac{R_U \cdot T}{\alpha_{an/cat} \cdot F} \operatorname{arcsinh} \left( \frac{i}{2 \cdot i_{0,an/cat} \cdot (1 - \theta)} \right) \quad (7)$$

Where  $\alpha_{an/cat}$  is the charge transfer coefficient (fitted parameter in

our model),  $i$  (in A/cm<sup>2</sup>) is the operating current density,  $i_{0,an/cat}$  (in A/cm<sup>2</sup>) is the exchange current density and  $\theta$  corresponds to the fractional bubble coverage of the electrode surface.

The evaluation of  $\theta$  value is very complex since depending of several parameters such as electrode surface characteristics, electrolyte surface tension, natural and forced circulation of the electrolyte. In the present study, the bubble rate coverage was expressed as a function of current density and temperature according to an empirical relationship reported by Hammoudi *et al.* [52]. A temperature-dependent Arrhenius expression was applied to evaluate the exchange current density [53]:

$$i_{0,an/cat} = \gamma_M \cdot i_{0,ref,an/cat} \cdot \exp \left[ \frac{-E_{a,act,an/cat} \cdot 10^3}{R_U} \cdot \left( \frac{1}{T} - \frac{1}{T_{ref}} \right) \right] \quad (8)$$

Where  $\gamma_M$  is the roughness factor,  $i_{0,ref,an/cat}$  (in A/cm<sup>2</sup>) is the reference exchange current density at the reference temperature  $T_{ref}$  (298.15 K) and  $E_{a,act,an/cat}$  (in kJ/mol) corresponds to the activation energy. The terms  $i_{0,ref,an/cat}$  and  $E_{a,act,an/cat}$  were considered as fitted parameters in the present model.

In order to compute the overall ohmic overpotential, the various contributions were modelled as electrical resistances:

$$V_{ohm} = ASR_{ohm} \cdot i = (ASR_{electric} + ASR_{KOHsol} + ASR_{mem}) \cdot i \quad (9)$$

Where  $ASR_{ohm}$  (in  $\Omega \cdot \text{cm}^2$ ) is the overall ohmic area specific resistance (ASR),  $ASR_{electric}$  (in  $\Omega \cdot \text{cm}^2$ ) is the electrical ASR due to contact and electrode resistances (which was treated as fitted parameter),  $ASR_{KOHsol}$  (in  $\Omega \cdot \text{cm}^2$ ) represents the ionic ASR due to the electrolyte and  $ASR_{mem}$  (in  $\Omega \cdot \text{cm}^2$ ) corresponds to the ionic ASR of the membrane.

The resistance of the membrane separator was computed according to the formula adopted by Abdin *et al.* [53], which depends on the membrane thickness, tortuosity, porosity and wettability factor (this last imposed as fitted parameter). The resistance of the electrolyte was derived starting from the ionic conductivity of the KOH solution as a function of temperature and molarity and corrected to take into account the gas void fraction according to the Bruggeman equation [47].

The diffusion overpotential was not considered for the alkaline electrolyzer because its effect is assumed to be negligible [50].

The Faraday's law, with the inclusion of the Faraday efficiency term, was employed to evaluate the amount of hydrogen produced by the electrolyzer. The following commonly employed expression was adopted for the estimation of the Faraday efficiency [54]:

$$\eta_F = \frac{i^2}{f_1 + i^2 \cdot f_2} \quad (10)$$

The parameters  $f_1$  and  $f_2$  were derived from Ulleberg [54], considering an operating temperature of 70 °C, which is the value we used during the simulations.

### 2.2.2. PEM electrolyzer

The reversible cell voltage was expressed as [55]:

$$V_{rev}(T, p) = V_{rev}(T, p_0) + \frac{R_U \cdot T}{2 \cdot F} \ln \left( \frac{(p_{cat} - p_{H_2O}) \cdot (p_{an} - p_{H_2O})^{0.5}}{p_{H_2O}} \right) \quad (11)$$

Where  $p_{H_2O}$  (in bar) corresponds to the water partial pressure, which is assumed to be equal to the water saturation pressure since gases produced during electrolysis are generally saturated with water vapour [56]. The water saturation pressure as a function of temperature was estimated according to the relationship reported by Balej [51].

Eq. (7) without the presence of the  $\theta$  term was used to compute the activation overvoltage. Analogously to the alkaline electrolyzer, the exchange current density was modelled by employing a temperature-dependent Arrhenius expression (Eq. (8)) [55].

The ohmic overpotential is caused by electrical and ionic resistances. The electrical contribution is due to the resistance of the electrically conductive components to the passage of electrons. The ionic one is

instead caused by protons flowing through the membrane. Most of electrical resistance is generally caused by the lack of proper contact between various components. However, ionic resistance is usually the major contributor [57]. The overall ohmic overpotential can be written as:

$$V_{\text{ohm}} = \text{ASR}_{\text{ohm}} \cdot i = (\text{ASR}_{\text{electric}} + \text{ASR}_{\text{mem}}) \cdot i \quad (12)$$

The electrical ASR ( $\text{ASR}_{\text{electric}}$ ) was treated as fitted parameter in the model calibration. The area specific resistance of the membrane to the proton flow ( $\text{ASR}_{\text{mem}}$ ) was instead computed starting from the membrane ionic conductivity, which is highly dependent on the operating temperature and the membrane water content. Analogously to the approach performed by Espinosa-López *et al.* [58] and García-Valverde *et al.* [59], the temperature dependence of the membrane ionic conductivity was expressed using an Arrhenius expression in the following form:

$$\sigma_{\text{mem}} = \sigma_{\text{mem,ref}} \cdot \exp \left[ \frac{-E_{a,\text{mem}} \cdot 10^3}{R_U} \left( \frac{1}{T} - \frac{1}{T_{\text{ref}}} \right) \right] \quad (13)$$

Where  $\sigma_{\text{mem,ref}}$  (in  $1/\Omega/\text{cm}$ ) is the reference membrane ionic conductivity at the reference temperature  $T_{\text{ref}}$  (298.15 K) and  $E_{a,\text{mem}}$  (in kJ/mol) is the activation energy that is required for the proton transport through the membrane. Both pre-exponential and exponential terms of Eq. (13) were derived by the model calibration.

Diffusion losses are caused by mass transport limitations, with consequent concentration gradient between the bulk flow and electrode/membrane interface. Diffusion losses are generally lower than the activation and ohmic ones. Their contribution is thus neglected in various studies [60]. However, their role can become relevant when operating at high current densities. In this work, the concentration overpotential is assumed to occur only at the anode side since its contribution is dominant compared to the cathode [59]. It was modelled by considering the limiting current density parameter:

$$V_{\text{diff,an}} = \frac{R_U \cdot T}{4 \cdot F} \cdot \ln \left( 1 - \frac{i}{i_{l,\text{an}}} \right) \quad (14)$$

Where  $i_{l,\text{an}}$  (in  $\text{A}/\text{cm}^2$ ) is the limiting current density at the anode, whose value was assumed to be  $6 \text{ A}/\text{cm}^2$  [61].

The Faraday efficiency (depending on the operating conditions, i.e., temperature, pressure and current) was evaluated as a function of the  $\text{H}_2$  and  $\text{O}_2$  fluxes across the membrane and the production rate of gases according to the following relationship [56,62]:

$$\eta_F = 1 - \frac{2 \cdot F}{i} \cdot \left( \dot{N}_{\text{H}_2,\text{tot}} + 2 \cdot \dot{N}_{\text{O}_2,\text{tot}} \right) \quad (15)$$

Where  $\dot{N}_{\text{H}_2,\text{tot}}$  and  $\dot{N}_{\text{O}_2,\text{tot}}$  (in  $\text{mol}/\text{cm}^2/\text{s}$ ) are the overall hydrogen and oxygen fluxes across the PEM membrane. In the above formula it is supposed that all the oxygen moving to the cathode is electrochemically reduced or catalytically react with hydrogen generating water. In order to evaluate  $\dot{N}_{\text{H}_2,\text{tot}}$  and  $\dot{N}_{\text{O}_2,\text{tot}}$ , both the diffusive and convective contributions of the  $\text{H}_2$  and  $\text{O}_2$  fluxes crossing the membrane were computed [63].

### 2.2.3. PEM fuel cell

The reversible cell voltage was evaluated according to the following expression [64–66]:

$$V_{\text{rev}}(T, p) = 1.228 - 0.85 \cdot 10^{-3} \cdot (T - 298.15) + 4.3086 \cdot 10^{-5} \cdot T \cdot \ln \left( p_{\text{H}_2,\text{an, ch}} \cdot p_{\text{O}_2,\text{cat, ch}}^{0.5} \right) \quad (16)$$

Where  $p_{\text{H}_2,\text{an, ch}}$  and  $p_{\text{O}_2,\text{cat, ch}}$  (in bar) correspond to the hydrogen and oxygen effective partial pressures at the anode and cathode channel, respectively. The effective oxygen partial pressure was approximated using a log-mean average of the oxygen partial pressure at the inlet and outlet. The arithmetic mean was instead used to compute the effective hydrogen partial pressure [66].

**Table 2**

Main technical input parameters to evaluate the performance curve of the  $\text{H}_2$ -based technologies.

	ALK EL	PEM EL	PEM FC
Operating temperature	70 °C [2]	60 °C [2]	60 °C [2]
Operating pressure	30 bar [2]	30 bar [2]	1 bar [2]
System minimum power (% of rated power)	15% [71]	10% [2]	6% [2]
Max. current density	0.35 $\text{A}/\text{cm}^2$ [67,68]	1.8 $\text{A}/\text{cm}^2$ [72]	1.2 $\text{A}/\text{cm}^2$ [2]
Aux. consumption in nominal condition (% of rated power)	10% [73]	10% [69,73]	8% [2]
Aux. consumption in stand-by (% of aux. nom. consumption)	29% [74]	29% [74]	50% [74]

The activation overvoltage term was evaluated according to Eq. (7), without the presence of the  $\theta$  parameter. Eq. (8) was used for the evaluation of the exchange current density.

Analogously to the PEM electrolyzer, Eq. (13) was applied to compute the membrane ionic conductivity and hence the membrane ASR. The total ohmic overpotential was then derived by employing Eq. (12).

The following concentration overvoltage term needs also to be added to take into account mass transport phenomena effects:

$$V_{\text{diff,an/cat}} = \frac{R_U \cdot T}{z_{\text{an/cat}} \cdot F} \cdot \ln \left( 1 - \frac{i}{i_{l,\text{an/cat}}} \right) \quad (17)$$

Where the  $z_{\text{an/cat}}$  parameter is equal to 2 and 4 at the anode and cathode side, respectively.  $i_{l,\text{an/cat}}$  (in  $\text{A}/\text{cm}^2$ ) stands for the limiting current density at the anode/cathode side.

### 2.2.4. Electrolyzer and fuel cell performance

Main input parameters used to evaluate the performance curve of the electrolyzer and fuel cell are reported in Table 2. The operating temperature and pressure were taken from [2]. Referring to the alkaline electrolyzer, the maximum achievable current density was set to  $0.35 \text{ A}/\text{cm}^2$ , in line with Refs. [67,68]. A maximum current density of  $1.8 \text{ A}/\text{cm}^2$  was instead considered for the PEM electrolyzer. This value is between  $1.7 \text{ A}/\text{cm}^2$  and  $2 \text{ A}/\text{cm}^2$ , which are reported by Mayyas *et al.* [69] and Parra *et al.* [67], respectively. Referring to the PEM fuel cell, the adopted value of  $1.2 \text{ A}/\text{cm}^2$  lies in the range  $1\text{--}1.5 \text{ A}/\text{cm}^2$  [49,70]. In order to move from the cell to the system efficiency curve, it is required to know the power consumption due to auxiliary components. It was assumed

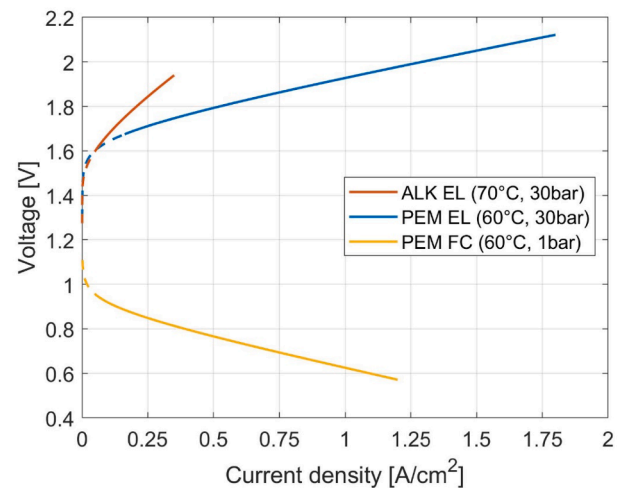


**Fig. 3.** Polarization curves of electrolyzer and fuel cell devices at the selected operating conditions.

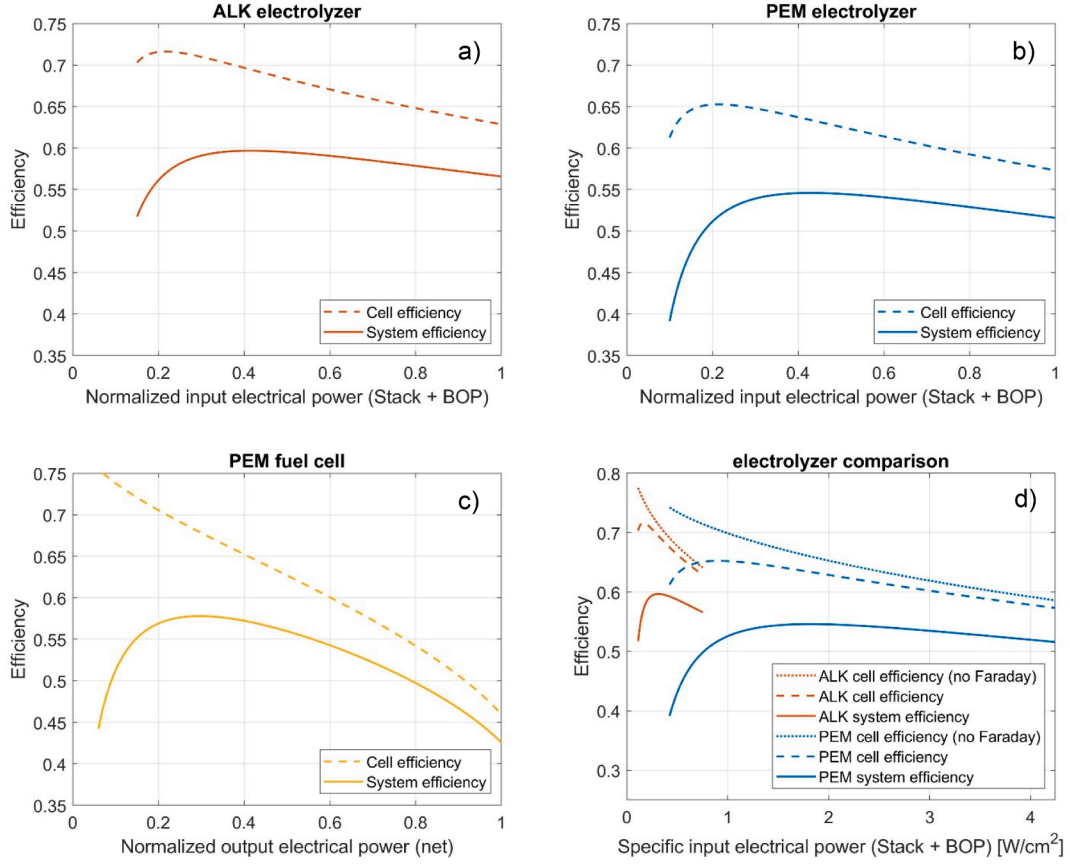


Fig. 4. Cell and system efficiency of the electrolyzer and fuel cell devices at the selected operating conditions.

auxiliary consumption to vary linearly from stand-by to nominal conditions.

For the sake of comparison, Fig. 3 reports the polarization curves of both alkaline and PEM electrolyzers and PEM fuel cell at the selected operating conditions. The PEM electrolyzer is able to operate at a much higher current density (i.e., hydrogen production per unit of active area), which also results in greater compactness of the PEM stack compared to the alkaline one. On the other hand, the alkaline technology is currently less expensive and with higher stack lifetime than PEM electrolysis.

Fig. 4a–c report the cell and system efficiency (on LHV basis) of the electrochemical devices as a function of the normalized operating power. Fig. 4d shows instead the cell and system efficiency of the alkaline and PEM electrolyzer as a function of the specific input electrical power (with no normalization). The cell efficiency curve without the Faraday efficiency term is also depicted. Nominal specific energy consumptions that were derived from the model are in line with values reported in the literature. Referring to the alkaline electrolyzer system, the obtained nominal value of 5.26 kWh/Nm<sup>3</sup> (i.e., LHV efficiency of 0.56) lies in the range 5.0–5.9 kWh/Nm<sup>3</sup> reported by Buttler *et al.* [68]. The specific energy consumption of 5.76 kWh/Nm<sup>3</sup> (i.e., LHV efficiency of 0.52) computed for the PEM electrolyzer system is also within the reported range of 5.0–6.5 kWh/Nm<sup>3</sup> [68]. Finally, referring to the PEM fuel cell, the nominal system efficiency of around 0.43 is close to what stated in [2].

The system efficiency curves were then approximated by means of polynomial fitted curves to be used in the optimal sizing problem.

### 2.3. Hydrogen and battery storage

The battery storage was modelled by means of the state-of-charge (SOC) term, representing the ratio between the total amount of energy

currently contained in the battery bank and the battery maximum capacity. It was defined according to the following relationship [2]:

$$\text{SOC}(t) = \text{SOC}(t-1) \cdot (1 - \sigma_{BT}) + \frac{P_{BT, ch}(t-1) \cdot \Delta t \cdot \eta_{BT, ch} \cdot \eta_{BT, conv}}{\text{Cap}_{BT}} - \frac{P_{BT, dc}(t-1) \cdot \Delta t}{\eta_{BT, dc} \cdot \eta_{BT, conv} \cdot \text{Cap}_{BT}} \quad (18)$$

Where  $\sigma_{BT}$  is the battery self-discharge coefficient,  $P_{BT, ch}$  and  $P_{BT, dc}$  (in kW) correspond to the battery charging and discharging power (at the DC bus level),  $\Delta t$  is the time step (in h)  $\text{Cap}_{BT}$  (in kWh) is the battery rated capacity,  $\eta_{BT, ch}$  and  $\eta_{BT, dc}$  are the battery charging and discharging efficiencies and  $\eta_{BT, conv}$  is the efficiency of the battery converter.

Similarly, the hydrogen tank was described by introducing the level-of-hydrogen (LOH) parameter, which is defined as the ratio between the total amount of energy currently contained in the hydrogen tank and its maximum capacity [2]:

$$\text{LOH}(t) = \text{LOH}(t-1) + \frac{P_{EL}(t-1) \cdot \Delta t \cdot \eta_{EL}}{\text{Cap}_{H_2}} - \frac{P_{FC}(t-1) \cdot \Delta t}{\eta_{FC} \cdot \text{Cap}_{H_2}} \quad (19)$$

Where  $P_{EL}$  and  $P_{FC}$  (in kW) correspond to the electrolyzer and fuel cell operating power (at the DC bus level),  $\text{Cap}_{H_2}$  (in kWh) is the hydrogen storage tank rated capacity,  $\eta_{EL}$  and  $\eta_{FC}$  are the electrolyzer and fuel cell efficiencies (already including converter losses).

Constraints on the SOC and LOH are given by:

$$\text{SOC}_{min} \leq \text{SOC}(t) \leq \text{SOC}_{max} \quad (20)$$

$$\text{LOH}_{min} \leq \text{LOH}(t) \leq \text{LOH}_{max} \quad (21)$$

The SOC should not go below  $\text{SOC}_{min}$  in order to avoid significant degradation of the battery component. The  $\text{LOH}_{min}$  limit must also be satisfied to allow hydrogen to be supplied to the fuel cell (it is computed

as the ratio between the minimum and maximum operating pressure of the H<sub>2</sub> tank).

### 2.4. Energy management strategy

Energy balance simulations have been carried out over a reference year with 1 h-time step resolution. An energy management strategy (EMS) needs thus to be developed to model the operation of the RES-based system. The detailed logical block diagram of the adopted rule-based EMS is reported in [2]. Batteries and the hydrogen equipment are allowed to intervene if the SOC and LOH values lie within their lower and upper boundaries, respectively. Electrolyzer and fuel cell are also forced to operate within their modulation ranges. In case the electrical demand is higher than the renewable power, priority of intervention is given to the battery discharging. The fuel cell device is then activated to cover the remaining energy deficit in order to avoid the over-discharging of the battery, i.e., keep the SOC parameter higher than  $SOC_{min}$ . Instead, in case the electrical demand is lower than the renewable power, the surplus RES energy is first used to charge the battery bank until reaching the maximum SOC, then converted into hydrogen through the electrolyzer and finally curtailed. In the considered EMS, batteries act thus as shorter-term storage operating first when required (and thus limiting the number of start-ups of the electrolyzer and fuel cell); whereas hydrogen works as longer-term storage medium intervening when the upper and lower operating limits of the battery are reached (so as to limit the degradation, and hence loss of performance, of the battery).

## 3. Optimal system sizing

### 3.1. Sizing method

The LPSP index over a given time period  $T$  (in this case, the whole year) was employed in order to evaluate the reliability of the off-grid system in covering the electrical load [23]:

$$LPSP = \frac{\sum_{t=1}^T P_{NS}(t) \cdot \Delta t}{\sum_{t=1}^T P_{LD}(t) \cdot \Delta t} \quad (22)$$

Where  $P_{LD}$  and  $P_{NS}$  (in kW) represent the electrical power demand and the demand fraction that is not satisfied at each time step  $t$ , respectively. An LPSP equal to 0 means that the load demand is satisfied at all times by the stand-alone power system throughout the year.

The objective function to be minimized by the sizing optimization is the levelized cost of energy. More in detail, the optimization methodology employs the PSO algorithm to search for the system configuration, i.e., sizes of the various components (PV, EL, FC, HT, BT), that allows to minimize the LCOE while satisfying the following reliability and sustainability constraints:

$$LPSP \leq LPSP^* \quad (23)$$

$$E_{BT}(t_{end}) \geq E_{BT}(t_{start}) \quad (24)$$

$$E_{H_2}(t_{end}) \geq E_{H_2}(t_{start}) \quad (25)$$

Where  $LPSP^*$  corresponds to the maximum allowed LPSP,  $E_{BT}$  (in kWh) is the energy stored in the battery and  $E_{H_2}$  (in kWh) is the energy stored in the form of hydrogen in the pressurized tank. A  $LPSP^*$  value of 0 is used to simulate a completely energy autonomous site. Eq. (24) and Eq. (25) verify that the stored energy within the BT and H<sub>2</sub> systems at the end of the year is not lower than the amount present at the beginning of the year [38]. The initial SOC and LOH were set to 0.5 in the present study.

Component sizes to be optimized are also forced to vary between specific lower and upper bounds (with  $i = \{PV, EL, FC, HT, BT\}$ ):

$$S_{i,min} \leq S_i \leq S_{i,max} \quad (26)$$

Where  $S_{i,min}$  is set to 0 for all the variables.

Concerning the PSO algorithm, a value of 100 was considered for the size of population and both the cognitive and social acceleration constants [7] were set to 2. During the PSO main loop, the velocities and position of the particles are iteratively updated until reaching one of the following stopping criteria: 1) reaching a maximum iteration number equal to  $It_{MAX}$  or 2) no changes in 30 iterations for the global best position (relative change less than  $10^{-6}$ ).  $It_{MAX}$  is the maximum number of iterations which should be chosen high enough so as not to be reached.

### 3.2. Objective function evaluation

The levelized cost of energy (in €/kWh) was computed as follows:

$$LCOE = \frac{C_{NPC,tot}}{\sum_{j=1}^{L_{PR}} \frac{E_{tot,j}}{(1+d)^j}} \quad (27)$$

Where  $C_{NPC,tot}$  (in €) is the total net present cost (NPC),  $E_{tot,j}$  (in kWh) corresponds to the total amount of energy provided by the RES + P2P system to the final user along the  $j$ -th year,  $L_{PR}$  is the project lifetime and  $d$  corresponds to the real discount rate, which was derived as [2]:

$$d = \frac{\dot{d} - ir}{1 + ir} \quad (28)$$

Where  $\dot{d}$  and  $ir$  stand for the nominal discount and inflation rate, respectively.

The total net present cost is given by the sum of the present value of all the costs incurred by the system (capital, O&M and replacement contributions) minus the present value of all the revenues (i.e., salvage contributions) over its lifetime:

$$C_{NPC,tot} = C_{inv,tot} + C_{NPC,OM,tot} + C_{NPC,rep,tot} - C_{NPC,sal,tot} \quad (29)$$

The investment and O&M terms were computed as follows (with  $i = PV, EL, FC, BT, HT$ ):

$$C_{inv,tot} = \sum_i C_{inv,i,0} \quad (30)$$

$$C_{NPC,OM,tot} = \sum_{j=1}^{L_{PR}} \frac{\sum_i C_{OM,i,j}}{(1+d)^j} \quad (31)$$

The replacement and salvage contributions were instead derived as (with  $i = EL, FC, BT$ ):

$$C_{NPC,rep,tot} = \sum_{j=1}^{L_{PR}} \frac{\sum_i C_{rep,i,j}}{(1+d)^j} \quad (32)$$

$$C_{NPC,sal,tot} = \sum_i \frac{C_{sal,i,L_{PR}}}{(1+d)^{L_{PR}}} \quad (33)$$

Where  $C_{inv,i,j}$ ,  $C_{OM,i,j}$ ,  $C_{rep,i,j}$  and  $C_{sal,i,j}$  (in €) correspond to the investment, O&M, replacement and salvage costs referred to the  $i$ -th component for the  $j$ -th year. Investment costs are performed at the beginning of the analysis period (i.e.,  $j=0$ ). The replacement cost of a certain  $i$ -th component is accounted for at the end of its lifetime (and no replacement is allowed at  $L_{PR}$  year). As described by Eq. (33), it is assumed the salvage cost to occur at the end of the project lifetime.

The salvage value represents the economic value of a component at the end of the analysis period ( $L_{PR}$ ) and it is supposed to be directly proportional to its remaining life. This term is considered for components that are potentially subjected to replacement (i.e., BT, EL and FC):

$$C_{sal,i} = C_{rep,i} \cdot \frac{L_{rem,i}}{L_i} \quad (34)$$

$L_i$  (in years) is the component lifetime; whereas  $L_{rem,i}$  (in years) is the remaining lifetime of the component at the end of the project lifetime and is given by (for  $L_i \neq L_{PR}$ ):

**Table 3**  
Main techno-economic input parameters for PV renewable generation systems.

PV power plant parameters		
Investment cost (mono-crystalline silicon)	1547 €/kW	[2]
Replacement cost (converter)	80 €/kW	[2]
Lifetime (PV panels)	Project lifetime	
Lifetime (converter)	10 years	[2]
O&M cost	24 €/kW/y	[2]
Derating factor ( $f_{PV}$ )	0.86	[46]
Nominal operating cell temperature (NOCT)	44 °C	[75]
Temperature coefficient ( $\gamma_T$ )	-0.003 1/K	[75]
PV surface slope ( $\beta$ )	34°	[46]
PV surface azimuth ( $\phi$ )	18°	[46]
Albedo of the ground ( $\rho_g$ )	0.2	[44]

**Table 4**  
Main techno-economic input parameters for the battery system.

Li-ion battery		
Investment cost (system)	550 €/kWh	[2,16]
Replacement cost (% of inv. cost)	50%	[76,77]
Lifetime of the battery bank	DOD-CTF	[78]
BOP lifetime	Project lifetime	
O&M cost	10 €/kWh/y	[79]
Charging efficiency ( $\eta_{BT,ch}$ )	0.95	[79,80]
Discharging efficiency ( $\eta_{BT,dc}$ )	0.95	[79,80]
Self-discharge ( $\sigma_{BT}$ )	5%/month	[16]
Maximum SOC ( $SOC_{max}$ )	1	
Minimum SOC ( $SOC_{min}$ )	0.2	[16,79]
Lead acid battery		
Investment cost (system)	250 €/kWh	[77]
Replacement cost (% of inv. cost)	50%	[76]
Lifetime of the battery bank	DOD-CTF curve	[81]
BOP lifetime	Project lifetime	
O&M cost	7€/kWh/y	[79]
Charging efficiency ( $\eta_{BT,ch}$ )	0.85	[16]
Discharging efficiency ( $\eta_{BT,dc}$ )	0.85	[16]
Self-discharge ( $\sigma_{BT}$ )	0.25%/day	[16]
Maximum SOC ( $SOC_{max}$ )	1	[16]
Minimum SOC ( $SOC_{min}$ )	0.5	[79]

$$L_{rem,i} = L_i - \left[ L_{PR} - L_i \cdot INT \left( \frac{L_{PR}}{L_i} \right) \right] \quad (35)$$

Where INT is a function that returns the integer amount of a real number.  $L_{rem,i}$  is zero in case  $L_i = L_{PR}$ .

Main input data for the techno-economic analysis are shown in Tables 3–5 for the PV, battery and hydrogen-based systems, respectively. Other techno-economic assumptions are reported in Table 6.

The scale dependencies of costs have been considered for the electrolyzer and fuel cell devices. The EL and FC investment costs were modelled by means of a power function in the following form (with  $i = EL, FC$ ):

$$c_{inv,i} = \left( \frac{S_i}{S_{ref,i}} \right)^{n_i} \cdot \frac{c_{inv,ref,i} \cdot S_{ref,i}}{S_i} \quad (36)$$

Where  $c_{inv,i}$  (in €/kW) represents the specific investment cost of the component, whose size is  $S_i$  (in kW). The term  $c_{inv,ref,i}$  (in €/kW) corresponds instead to the specific investment cost of the same equipment with reference size  $S_{ref,i}$  (in kW). The term  $n_i$  stands for the cost exponent of the power function. The values adopted for these parameters are reported in Table 5. Referring to the alkaline electrolyzer, the reference specific investment cost of 2000 €/kW was taken from [85] considering a reference size of 312 kW. The cost exponent  $n$  was set equal to 0.65 to be in agreement with the cost trend reported by Proost [82]. A reference specific cost of 4600 €/kW for a size of 50 kW with a cost exponent of

**Table 5**  
Main techno-economic input parameters for the hydrogen-based system.

Hydrogen tank		
Investment cost	470 €/kg	[71]
O&M cost (% of inv. cost)	2%	[71]
Lifetime	Project lifetime	
Minimum pressure	3 bar	[2]
Maximum pressure	28 bar	[2]
PEM electrolyzer		
Ref. specific cost ( $c_{inv,ref}$ )	4600 €/kW	[82]
Ref. size ( $S_{ref}$ )	50 kW	[82]
Cost exponent ( $n$ )	0.65	
Stack replacement cost (% of inv. cost)	26.7%	[83,84]
O&M cost (fixed) (% of inv. cost)	1/3·(4%)	[71]
O&M cost (variable) (% of inv. cost)	2/3·(4%)	[71]
BOP lifetime	Project lifetime	
Efficiency degradation	0.25%/1000 h	[71]
Operating hours ( $N_{h,tot,EL}$ )	40,000 h	[71]
On-off cycle number ( $N_{st,tot,EL}$ )	5000	[83]
Alkaline electrolyzer		
Ref. specific cost ( $c_{inv,ref}$ )	2000 €/kW	[85]
Ref. size ( $S_{ref}$ )	312 kW	[85]
Cost exponent ( $n$ )	0.65	
Stack replacement cost (% of inv. cost)	26.7%	[83,84]
O&M cost (fixed) (% of inv. cost)	1/3·(4%)	[71]
O&M cost (variable) (% of inv. cost)	2/3·(4%)	[71]
BOP lifetime	Project lifetime	
Efficiency degradation	0.13%/1000 h	[71]
Operating hours ( $N_{h,tot,EL}$ )	76,923 h	[71]
On-off cycle number ( $N_{st,tot,EL}$ )	7500	[86]
PEM fuel cell		
Ref. specific cost ( $c_{inv,ref}$ )	3947 €/kW	[87]
Ref. size ( $S_{ref}$ )	10 kW	[87]
Cost exponent ( $n$ )	0.7	[67]
Stack replacement cost (% of CAPEX)	26.7%	[83,84]
O&M cost (fixed) (% of CAPEX)	1/3·(4%)	[71]
O&M cost (variable) (% of CAPEX)	2/3·(4%)	[71]
BOP lifetime	Project lifetime	
Operating hours ( $N_{h,tot,FC}$ )	30,000 h	[33,38]
On-off cycle number ( $N_{st,tot,FC}$ )	10,000	[88]

**Table 6**  
Other techno-economic assumptions.

Other techno-economic assumptions		
Nominal discount rate ( $d$ )	7%	[2]
Inflation rate ( $ir$ )	2%	[2]
Project lifetime ( $L_{PR}$ )	20 years	
DC/DC converter efficiency	0.965	[74]
DC/AC converter efficiency	0.955	[74]

0.65 was instead considered for the PEM electrolyzer [82]. The fuel cell specific cost of 3947 €/kW was taken from [87] considering a reference size of 10 kW. The cost exponent  $n$  was set equal to 0.7 in agreement with previous studies [67]. The cost curve thus obtained is in accordance with values from [16] and [89].

The O&M cost referred to electrolyzer and fuel cell systems is assumed to be 4% of the total system investment cost. It is composed of 1/3 fixed and 2/3 variable contributions, similarly to what reported in Ref. [71]. The variable costs are supposed to be proportional to the EL/FC operating time, as described by the following relationship (with  $i = EL, FC$ ):

$$c_{OM,i,var} = \frac{2}{3} \frac{4}{100} \cdot c_{inv,i} \cdot \frac{N_{h,yr,i}}{8760} \quad (37)$$

Where  $c_{OM,i,var}$  (in €/kW) corresponds to the annual O&M cost per

**Table 7**  
Li-ion battery: Cycles to failure versus depth-of-discharge [78].

Depth of discharge (%)	Cycles to failure
50	50.00
70	3000
80	2500

**Table 8**  
Lead-acid battery: Cycles to failure versus depth-of-discharge [81].

Depth of discharge (%)	Cycles to failure
10	5700
25	2100
35	1470
50	1000
60	830
70	700
80	600
90	450

unit of size of the EL/FC component and  $N_{h,yr,i}$  is the yearly number of operating hours of the EL/FC (which depend on the simulation).

BT, EL and FC lifespan values are needed so as to know when their replacement occurs for a proper evaluation of the replacement and salvage costs. In the literature, the lifetime of components is often treated as a value known a-priori and imposed as an initial input data of the techno-economic analysis. In this study lifespan of components potentially subjected to replacement (i.e., battery bank and EL/FC stacks) was instead derived according to how they operate along the reference year.

The battery life was evaluated by computing the total amount of energy that can flow throughout it, i.e., the lifetime throughput (LT). This parameter was estimated starting from the lifetime curve, which is provided by the battery manufacturer. The curve shows different depth-of-discharge (DOD) values and the related cycles-to-failure (CTF). The lifetime throughput was obtained as [81]:

$$LT = \sum_{i=1}^n \frac{2 \cdot Cap_{BT} \cdot DOD_i \cdot CTF_i}{n} \quad (38)$$

Where  $Cap_{BT}$  (in kWh) is the battery rated capacity,  $DOD_i$  and  $CTF_i$  correspond to the DOD and CTF values of the  $i$ -th point of the lifetime curve, respectively and the term  $n$  stands for the number of points in the lifetime curve.

The battery lifetime can be then derived as:

$$L_{BT} = \min\left(\frac{LT}{AT}, L_{PR}\right) \quad (39)$$

Where  $AT$  (in kWh), i.e., the annual throughput, represents the energy flowing throughout the battery along the year and can be evaluated at the end of the yearly time horizon as:

$$AT = \sum_{t=1}^{8760} \left( P_{BT,ch}(t) \cdot \eta_{BT,ch} \cdot \eta_{BT,conv} + \frac{P_{BT,dc}(t)}{\eta_{BT,dc} \cdot \eta_{BT,conv}} \right) \quad (40)$$

Referring to Li-ion (LI) batteries, data for the lifetime throughput evaluation were taken from Zia *et al.* [78] and are shown in Table 7. They are in accordance with what reported by Few *et al.* [90], who stated around 2500 cycles at 80% DOD, and May *et al.* [91]. Lifetime curve values for the lead acid (LA) battery, from Bordin *et al.* [81], are instead displayed in Table 8.

The electrolyzer stack replacement is usually planned when the energy efficiency drops to 90% of its initial nominal value [71]. The same considerations are also valid for the fuel cell stack [92]. Referring to the electrolyzer, the total amount of working hours was computed by considering the efficiency degradation over time with continuous operation. By supposing an efficiency degradation of 0.13%/1,000 h for

the PEM EL and 0.25%/1000 h for the ALK EL [71] and imposing the stack replacement when efficiency goes below 90% of its initial value, the total amount of operating hours is around 80,000 and 40,000 h for the alkaline and PEM stacks, respectively. A value of 30,000 h was instead supposed for the PEM fuel cell stack lifetime [33,38]. As well as by the number of working hours of continuous operation, the EL/FC lifetime is also affected by the number of start-ups. A value of 5000 on/off switching cycles was reported by Santos *et al.* [83] referring to the PEM electrolyzer. The alkaline device is instead reported to tolerate around 5000–10,000 start/stop cycles [86]. A value of 7500 cycles was then taken as an average in the present study. Finally, referring to the PEM fuel cell, Torreglosa *et al.* [88] stated that a FC start-up corresponds to approximately 3 working hours in continuous operation.

The lifetime of the electrolyzer and the fuel cell was computed based on the effective number of operating hours and start-ups occurring during the year according to the simulation. The following formula was adopted (with  $i = EL, FC$ ):

$$L_i = \min\left(\left(\frac{N_{h,yr,i}}{N_{h,tot,i}} + \frac{N_{st,yr,i}}{N_{st,tot,i}}\right)^{-1}, L_{PR}\right) \quad (41)$$

Where  $N_{h,tot,i}$  and  $N_{st,tot,i}$  represent the total amount of working hours and start-ups of the EL/FC component during its lifetime, respectively. The terms  $N_{h,yr,i}$  and  $N_{st,yr,i}$  correspond instead to the number of working hours and start-ups of the EL/FC occurring during the yearly simulation, respectively.

As shown by Eqs. (39) and (41), the lifetime of the battery and H<sub>2</sub>-based components is set equal to the project lifetime if the computed lifespan value is higher than the project lifetime.

#### 4. Reference case study

The sizing optimization is performed on a renewable P2P system assumed to be installed in Ginostra, village on the Stromboli island in southern Italy [2]. The site is completely off-grid since not connected to neither the Italian grid nor the main Stromboli island microgrid. Currently, the site load is covered exclusively by the usage of diesel generators. The final cost of electrical energy is thus heavily dependent on the cost of fossil fuel, its logistic and transportation (which is only possible by helicopter due to the remoteness of the area). Being diesel genset the only source of electricity generation, any failure to the power system would expose the inhabitants to the possibility of a prolonged period of absence of the electrical service. It is therefore of great interest for the site to maximize the exploitation of local RES with the aim of increasing the reliability of the power supply service and decrease the current LCOE value. The investigation of different typologies of electrical energy storage solutions becomes hence essential to ensure high level of RES penetration and try to achieve the complete energy independence.

Input data used in this work for the Ginostra site, namely the hourly profiles along the year of the solar irradiance on the PV plane (in kW/m<sup>2</sup>), ambient temperature (in °C) and electrical demand (in kW), are shown in Fig. 5. PVGIS is used to evaluate the meteorological data, referring to a TMY. Hourly electrical load data are instead taken from [2]. The total yearly electrical demand to be covered is around 172 MWh. The load is characterized by a relevant seasonal variation (with a summer peak load slightly higher than 60 kW) because of the increased power consumption due to summer tourism.

#### 5. Results and discussion

Main results from the sizing optimization are reported in Table 9. Table 10 shows instead the main technical KPIs for the various renewable P2P configurations: lifetimes of P2P devices and number of yearly operating hours and start-ups of the electrolyzer and fuel cell. A graphical comparison of the LCOE of all the investigated configurations

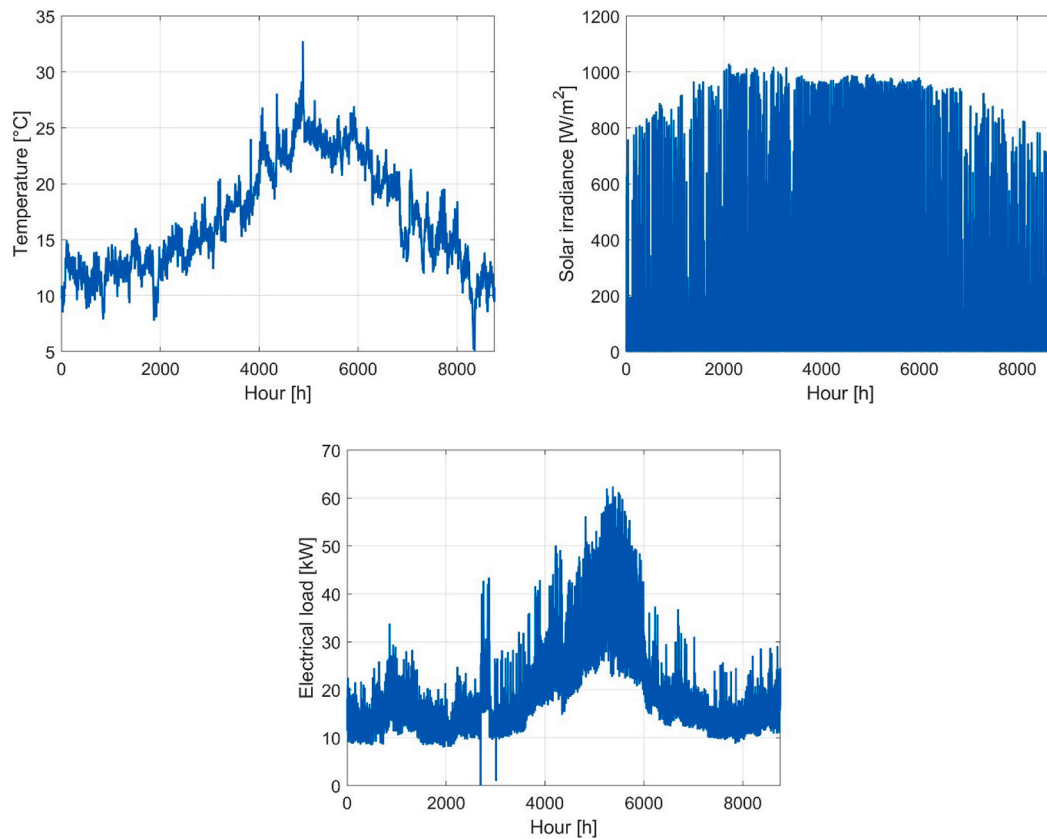


Fig. 5. Input data (meteorological and load) for the simulation of Ginostra site: ambient temperature, solar irradiance and electrical load at a resolution of 1 h.

Table 9  
Sizing results and LCOE values for the different renewable P2P configurations.

Configurations	PV [kW]	EL [kW]	FC [kW]	HT [kWh]	BT [kWh]	LCOE [€/kWh]
C1. PV + LA BT	336	-	-	-	1331	0.654
C2. PV + LI BT	285	-	-	-	948	0.548
C3. PV + H2 (PEM EL)	320	154	64	9753	-	0.844
C4. PV + H2 (ALK EL)	310	163	64	9519	-	0.743
C5. PV + LA BT + H2 (PEM EL)	209	5	30	4375	959	0.613
C6. PV + LA BT + H2 (ALK EL)	213	12	33	3562	809	0.608
C7. PV + LI BT + H2 (PEM EL)	205	8	33	3493	593	0.521
C8. PV + LI BT + H2 (ALK EL)	203	9	33	3366	592	0.510

is displayed in Fig. 6, where it is also reported how the different components contribute to the overall LCOE. Configurations 1 and 2 rely only on batteries as energy storage medium. The third and fourth configuration instead use hydrogen to store the surplus renewable energy.

Finally, the remaining ones present a hybrid storage, i.e., with both batteries and hydrogen.

Generally, it can be observed that the usage of Li-ion batteries is more convenient than the lead-acid technology. As summarized in

Table 10  
Main technical KPIs for the different renewable P2P configurations.

Configurations	$N_{h,yr,EL}$ [h]	$N_{st,yr,EL}$ [-]	$L_{EL}$ [yr]	$N_{h,yr,FC}$ [h]	$N_{st,yr,FC}$ [-]	$L_{FC}$ [yr]	$L_{BT}$ [yr]
C1. PV + LA BT	-	-	-	-	-	-	7
C2. PV + LI BT	-	-	-	-	-	-	NR*
C3. PV + H2 (PEM EL)	2794	417	7	5200	394	5	-
C4. PV + H2 (ALK EL)	2647	420	11	5214	396	5	-
C5. PV + LA BT + H2 (PEM EL)	1563	304	10	140	20	NR*	5
C6. PV + LA BT + H2 (ALK EL)	1267	251	NR*	266	57	NR*	4
C7. PV + LI BT + H2 (PEM EL)	1527	292	10	225	47	NR*	13
C8. PV + LI BT + H2 (ALK EL)	1371	266	19	228	48	NR*	13

\*NR: No replacement.

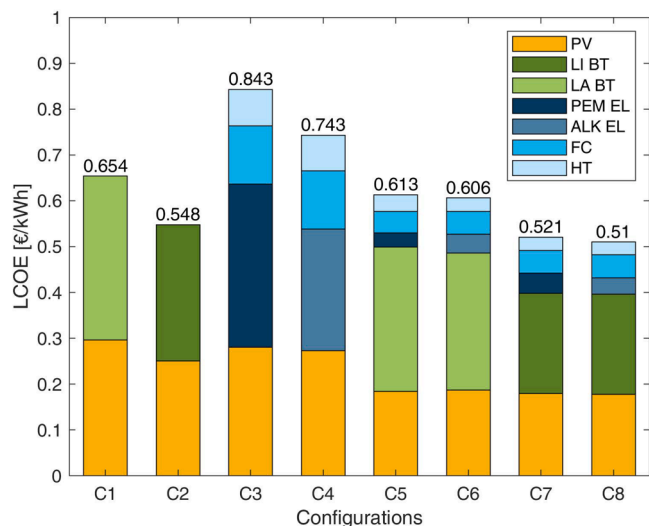


Fig. 6. Contributions to LCOE for the various renewable P2P configurations.

Table 4, despite the higher specific investment costs, LI BTs are in fact characterized by a higher roundtrip efficiency, lower self-discharge rate, higher lifetime and wider cycling modulation range than LA BTs. As an example, referring to the first two configurations, the LCOE moves from 0.65 to 0.55 €/kWh when changing from LA to LI batteries. The lithium-ion technology allows in fact to have lower PV panel nominal size (285 kW instead of 336 kW) and battery rated capacity (948 kWh instead of 1331 kWh). Moreover, as shown in Table 10, unlike the lead-acid technology (C1), no replacement is required for the LI battery bank (C2) during the course of the project lifetime.

Comparing C1 and C2 to C3 and C4 configurations, it can be noticed that a stand-alone power system with only batteries as energy storage is currently cheaper than a configuration relying only on hydrogen. Focusing on the hydrogen-based configuration, as clearly shown by C3 and C4 sizing results, alkaline electrolyzers are a more cost-effective choice with respect to PEM devices. A leveled cost of energy of approximately 0.84 €/kWh is obtained in case a PEM-type electrolyzer is considered. The LCOE drops to 0.74 €/kWh for the P2P system with alkaline electrolyzers, thanks to their lower cost and higher durability (the frequency of stack replacement is found to be every 11 years and 7 years for the alkaline and PEM electrolyzers, respectively, as displayed in Table 10).

As shown by the sizing outcomes of configurations 5–8, the energy storage hybridization (i.e., both battery and hydrogen) allows obtaining the cheapest RES-based power system configuration. Concerning a

system with Li-ion batteries, the inclusion of hydrogen leads to a LCOE reduction from 0.55 €/kWh to around 0.52 and 0.51 €/kWh when PEM and alkaline electrolyzers are employed, respectively. Similarly, the LCOE value of 0.65 €/kWh of C1 (LA BT) drops to approximately 0.60–0.61 €/kWh if batteries are coupled with hydrogen to store the excess renewable energy. In fact, the presence of hydrogen makes it possible to avoid the battery over-sizing: as an example, the LI BT rated capacity moves from 948 kWh for configuration 2 to around 590 kWh for the hybrid storage cases. Moreover, when considering both BT and H<sub>2</sub>, the required installed PV rated power also decreases, from roughly 300 to 200 kW, thus meaning that the local renewable resource is better exploited. The lower cost share attributed to the PV component for configurations with storage hybridization (i.e., C5 to C8) can be graphically observed in Fig. 6.

It is noteworthy that the usage of lifetime values depending on the P2P system operation along the reference year (i.e., by employing Eq. (39) and Eq. (41)) leads to a more precise estimation of the LCOE. As an example, when considering only hydrogen (i.e., C3–C4), the fuel cell lifetime becomes around 5 years, which coincides with a commonly adopted value in techno-economic evaluations [2]. If instead batteries are coupled with hydrogen, this results in lower usage of the H<sub>2</sub>-based components with consequent no necessity to replace the FC stack over the course of project lifetime. Similarly, the electrolyzer lifespan improves as well when considering the hybridization of the storage medium (with no stack replacement occurring only for configuration 6). Unlike the H<sub>2</sub>-based devices, the battery component shows a higher lifetime when considering a power system including only batteries, which is due to the battery over-sizing.

The resulting optimal HT capacities are in line with sizes considered within the framework of the REMOTE project [41] (whose sizes have been authorized in different European countries: Italy, Greece and Norway). However, as a general consideration, in case of excessive storage capacity and consequent safety (e.g., Seveso-III directive) or space issues, an upper limit on the storage capacity could be set during the optimal sizing process. Problems of space unavailability could also be faced by increasing the H<sub>2</sub> storage pressure (with inclusion of a compressor after the electrolyzer). The level of hydrogen trend along the year is reported in Fig. 7 for configurations 4 and 8, both of which rely on alkaline electrolyzers to produce hydrogen. The LOH graphs referred to the PEM EL device are analogous. A value of 0.5 was imposed for the LOH at the beginning of the year. It can be noticed the LOH at the end of the reference year to reach again the initial value as described by the sustainability constraint of Eq. (25). When only hydrogen is employed to store the surplus renewable energy, a H<sub>2</sub> storage rated capacity of slightly more than 9500 kWh is required (C4). The hydrogen storage capacity is around three times lower when both batteries and hydrogen are included within the off-grid power system (C8). However, for both

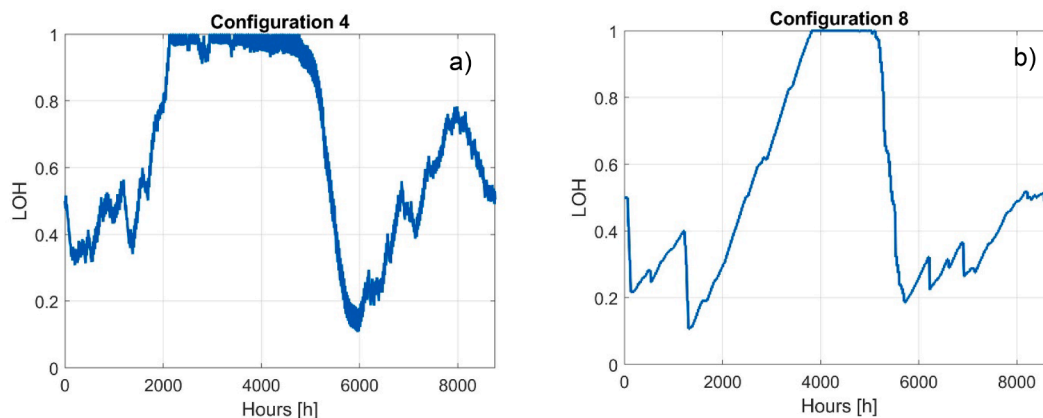


Fig. 7. LOH along the year for configuration 4 with PV + H<sub>2</sub> (H<sub>2</sub> capacity of 9519 kWh) and configuration 8 with PV + LI BT + H<sub>2</sub> (H<sub>2</sub> capacity of 3366 kWh). In both configuration the electrolyzer is of alkaline type.

configurations it is clearly visible the hydrogen long-term storage capability: the pressurized tank is filled with hydrogen earlier in the year; the LOH then sharply decreases during summer to face the increase in the electrical load due to tourism. Referring to the hybrid storage case (Fig. 7b), the initial LOH increase is more gradual. The main function of the electrolyzer is in fact to guarantee the H<sub>2</sub> tank to be full for the start of the summer season. It is thus not required to have an electrolyzer with high nominal size since the EL device can gradually fill the H<sub>2</sub> tank along the spring period. Instead, concerning configuration 4 (Fig. 7a), the fuel cell has to be used more continuously since it is the only power source when local RES is not enough to cover the load. The H<sub>2</sub> storage capacity and the electrolyzer size are therefore higher (the EL size is around 163 kW and 9 kW for C4 and C8, respectively). It can be also noticed that the LOH line is more scattered for C4 than for C8 due to the fuel cell intervention which is more frequent for C4 (the yearly number of fuel cell start-ups is 396 and 48 for C4 and C8, respectively).

The LCOE referred to the current configuration based on diesel generators is around 0.86 €/kWh [2]. This high electricity generation cost is strongly affected by the fuel transportation cost, which is around 2 €/L because of the site remoteness (fuel transportation is performed mainly by helicopter due to the geographical location of the Ginostra site). The analysed renewable P2P systems are thus more economically competitive than the exiting fossil fuel-based option, even considering the most expensive configurations relying only on local RES and hydrogen (around 0.84 €/kWh referring to the case with PEM electrolyzers). Moreover, besides the proven economic profitability, environmental advantages are also associated to these types of stand-alone renewable power systems since they allow to significantly reduce the emission of pollutants. In order to evaluate the amount of CO<sub>2</sub> released in the current diesel-based scenario, for each hour along the year the diesel fuel consumption was computed by applying the relationship adopted by Marocco et al. [2], which is function of both the diesel rated and operating power (the rated power was assumed equal to the load peak power). The overall yearly fuel consumption was then derived by the sum of the various hourly contributions. The annual amount of CO<sub>2</sub> released by the power system was thus calculated by considering the CO<sub>2</sub> emission coefficient for the diesel fuel consumption, which was assumed equal to 3 kg/L in agreement with Jakhriani et al. [93]. It is found that approximately 286 tons of CO<sub>2</sub> are at present emitted per year by using diesel generators in Ginostra. Their release could be avoided by employing a renewable P2P system, such as those presented in this work.

## 6. Conclusion

A methodology for the optimal sizing of a stand-alone renewable P2P system has been developed by means of the PSO technique. Detailed electrochemical models of the electrolyzer and fuel cell devices were implemented within the optimization process. Lifetimes of components were also computed based on their operating schedule. The sizing methodology was then applied to the off-grid village of Ginostra. Different typologies of batteries (Li-ion and lead-acid) and electrolyzers (alkaline and PEM) were investigated to provide a wider overview on different technology options for a P2P system in off-grid remote areas.

## Appendix

### Parameters of electrolyzer and fuel cell models

As described in Section 2.2, the calibration of the models was performed by minimizing the sum of the squares of the differences between experimental and related model voltage values.

Referring to the alkaline electrolyzer model, the resulting fitted parameters (see Table A1) allow obtaining a maximum relative error on voltage of around 1.28%. Values for the charge transfer coefficient ( $\alpha$ ) are reported to be in the range 0–2 and 0–1 for the anode and cathode, respectively [94]. The anodic and cathodic reference exchange current densities ( $i_{0,ref}$ ) are expected to lie in the range  $10^{-11}$ – $10^{-7}$  and  $10^{-4}$ – $10^{-1}$  A/cm<sup>2</sup>, respectively [53].

The adoption of Li-ion battery is currently a better economic choice compared to the lead acid-alternative even though investment and O&M costs of Li-ion batteries are higher. Concerning the H<sub>2</sub>-based energy system, alkaline electrolyzers are at present more cost-effective than PEM devices because of the lower cost and higher durability. However, the PEM electrolyzer is characterized by greater compactness and better dynamic performance (which is positive when coupled with highly intermittent RES). Local RES coupled with battery and/or hydrogen were found to be cost-competitive with respect to the current power system based on diesel generators. A configuration relying only on batteries (0.55–0.65 €/kWh) is cheaper than a system with only hydrogen (0.74–0.84 €/kWh). However, the cheapest configuration is the one with both batteries and hydrogen since it allows to avoid battery over-sizing and to better exploit the local source of solar energy. The presence of hydrogen is required due to its longer-term storage capability which enable to cope with the increase of the electrical load in the summer period. The configuration with a hybrid storage including Li-ion batteries and alkaline electrolyzers was shown to be the cheapest option with a levelized cost of energy of around 0.51 €/kWh. The LCOE of the current diesel-based system is instead higher (approximately 0.86 €/kWh), mainly because of the high fossil fuel cost due to transportation and logistic issues in remote locations. Moreover, environmental benefits related to renewable generation systems make these solutions even more attractive. Avoiding the usage of diesel generators would in fact allow to reduce or even eliminate the related CO<sub>2</sub> emissions. Approximately 286 tons of CO<sub>2</sub> are released each year due to diesel fuel consumption in the Ginostra site. Considering that diesel engines are still the dominant technology for electricity generation in off-grid areas, there is thus a high potential for reducing pollutants by introducing these kinds of renewable P2P systems.

### CRedit authorship contribution statement

**Paolo Marocco:** Conceptualization, Methodology, Software, Validation, Formal analysis, Investigation, Data curation, Writing - original draft, Visualization. **Domenico Ferrero:** Validation, Writing - review & editing, Supervision. **Andrea Lanzini:** Validation, Writing - review & editing, Supervision. **Massimo Santarelli:** Writing - review & editing, Supervision, Project administration, Funding acquisition.

### Declaration of Competing Interest

The authors declare that they have no known competing financial interests or personal relationships that could have appeared to influence the work reported in this paper.

### Acknowledgements

This project has received funding from the Fuel Cells and Hydrogen 2 Joint Undertaking under grant agreement No 779541. This Joint Undertaking receives support from the European Union's Horizon 2020 research and innovation programme, Hydrogen Europe and Hydrogen Europe research. The authors want to thank Enel Green Power in terms of input data for the modelling.

Reported values for the activation energy can be up to around 80 kJ/mol at the anode and 50 kJ/mol at the cathode [53]. A membrane wettability factor ( $\omega_{mem}$ ) of around 0.8–0.9 was found by Abdin et al. [53]. The values we found by the model calibration lie within the above cited ranges.

Main parameters referred to the PEM electrolyzer model are shown in Table A2. By performing the calibration process, the maximum relative error (modelled voltage with respect to experimental voltage) is approximately 1.55%. The fitted values for the charge transfer coefficients ( $\alpha$ ) lie within common ranges reported in the literature (around 0–2 for the anode and 0–1 for the cathode [96]). The anode and cathode reference exchange current density values ( $i_{0,ref}$ ) obtained from the calibration process are in accordance with values adopted by other studies and summarized by Carmo et al. [97]. The pre-exponential ( $\sigma_{mem,ref}$ ) and exponential ( $E_{a,mem}$ ) terms of the membrane ionic conductivity are also well in line with conductivity values estimated by an alternative relationship reported in Refs. [98,99] (when considering the membrane exposed to liquid water). Finally, the fitted values

**Table A1**

Fitted and fixed parameters for the alkaline cell electrolyzer model (the latter from Refs. [47,53,54,95]).

Fitted parameters	Value
$ASR_{electric}$	0.17 $\Omega \cdot \text{cm}^2$
$E_{a,act,an}$	82.27 kJ/mol
$E_{a,act,cat}$	32.76 kJ/mol
$i_{0,ref,an}$	$9.83 \cdot 10^{-8} \text{ A/cm}^2$
$i_{0,ref,cat}$	$7.32 \cdot 10^{-3} \text{ A/cm}^2$
$\alpha_{an}$	0.99
$\alpha_{cat}$	0.92
$\omega_{mem}$	0.81
Fixed parameters	
$f_1$	225
$f_2$	0.9825
$T_{ref}$	298.15 K
$\gamma_{M,an}$	2.5
$\gamma_{M,cat}$	1.5
Distance an. electrode-membrane	0 cm
Distance cat. electrode-membrane	0 cm
Membrane thickness	0.05 cm
KOH weight percentage	30%
Membrane porosity	0.42
Membrane tortuosity	2.18

**Table A2**

Fitted and fixed parameters for the PEM cell electrolyzer model (the latter from Refs. [61,100]).

Fitted parameters	Value
$ASR_{electric}$	$7.48 \cdot 10^{-2} \Omega \cdot \text{cm}^2$
$E_{a,act,an}$	59.95 kJ/mol
$E_{a,act,cat}$	8.57 kJ/mol
$E_{a,mem}$	10.32 kJ/mol
$i_{0,ref,an}$	$4.38 \cdot 10^{-9} \text{ A/cm}^2$
$i_{0,ref,cat}$	$4.94 \cdot 10^{-3} \text{ A/cm}^2$
$\alpha_{an}$	0.69
$\alpha_{cat}$	0.56
$\sigma_{mem,ref}$	0.106 1/ $\Omega$ /cm
Fixed parameters	
$i_{i,an}$	6 A/cm <sup>2</sup>
$T_{ref}$	298.15 K
An. catalyst density*	22.56 g/cm <sup>3</sup>
Cat. catalyst density*	21.45 g/cm <sup>3</sup>
An. catalyst crystallite diameter*	$2.9 \cdot 10^{-7} \text{ cm}$
Cat. catalyst crystallite diameter*	$2.7 \cdot 10^{-7} \text{ cm}$
An. catalyst fraction in contact with ionomer*	0.75
Cat. catalyst fraction in contact with ionomer*	0.75
An. catalyst loading*	0.001 g/cm <sup>2</sup>
Cat. catalyst loading*	0.0003 g/cm <sup>2</sup>
Membrane thickness	0.0183 cm

\*Parameter used to derive the roughness factor [100]

**Table A3**

Fitted and fixed parameters for the PEM cell fuel cell model (the latter from Refs. [49,57,66,100,101]).

Fitted parameters	Value
$ASR_{electric}$	$2.96 \cdot 10^{-2} \Omega \cdot \text{cm}^2$
$E_{a,act,an}$	19.92 kJ/mol
$E_{a,act,cat}$	70.09 kJ/mol
$E_{a,mem}$	9.82 kJ/mol
$i_{0,ref,an}$	$4.6 \cdot 10^{-3} \text{ A/cm}^2$
$i_{0,ref,cat}$	$1.39 \cdot 10^{-8} \text{ A/cm}^2$
$\alpha_{an}$	0.44
$\alpha_{cat}$	0.74
$\sigma_{mem,ref}$	0.070 1/ $\Omega$ /cm
Fixed parameters	
$i_{i,an}$	2 A/cm <sup>2</sup>
$i_{i,cat}$	2 A/cm <sup>2</sup>
$T_{ref}$	298.15 K
An. catalyst density*	21.45 g/cm <sup>3</sup>
Cat. catalyst density*	22.56 g/cm <sup>3</sup>
An. catalyst crystallite diameter*	$2.7 \cdot 10^{-7} \text{ cm}$
Cat. catalyst crystallite diameter*	$2.9 \cdot 10^{-7} \text{ cm}$
An. catalyst fraction in contact with ionomer*	0.75
Cat. catalyst fraction in contact with ionomer*	0.75
An. catalyst loading*	0.0003 g/cm <sup>2</sup>
Cat. catalyst loading*	0.001 g/cm <sup>2</sup>
Membrane thickness	0.0183 cm
An. hydrogen excess	1.2
Cat. air excess	2
An. relative humidity	0.5
Cat. relative humidity	1

\*Parameter used to derive the roughness factor [100]

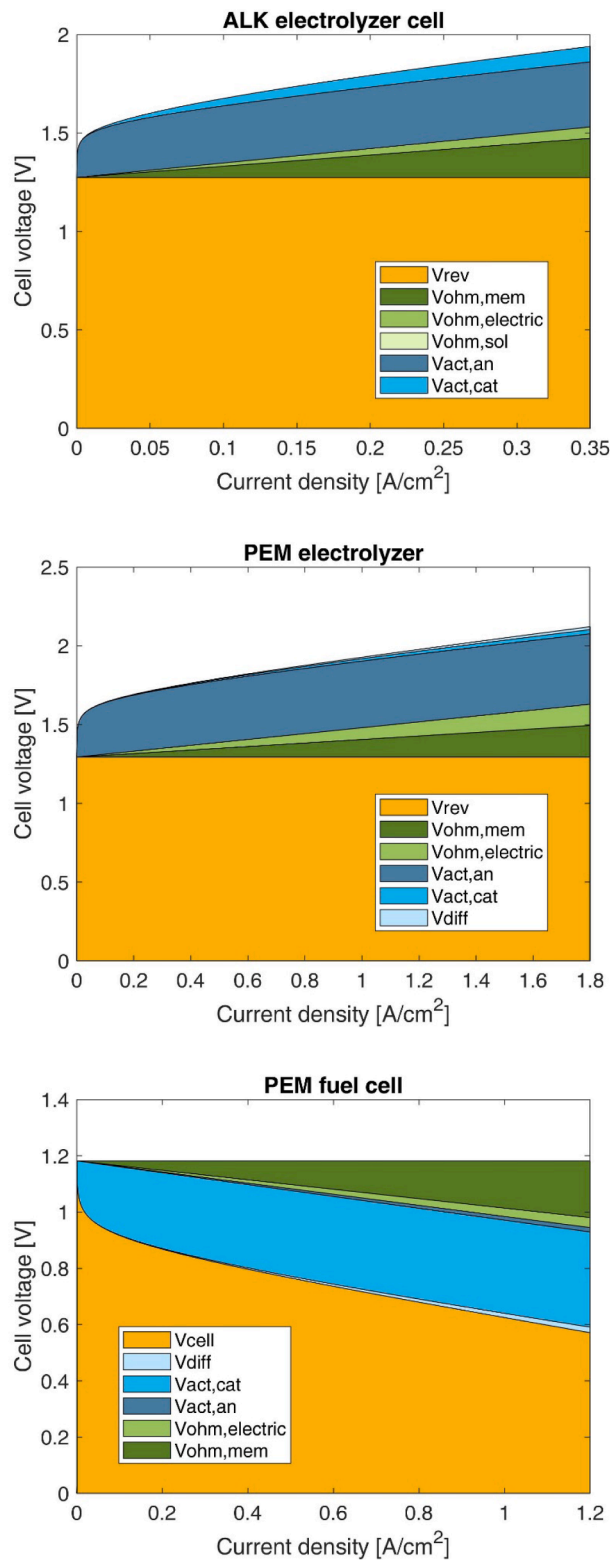


Fig. A1. Contributions of the various overpotentials to the ALK electrolyzer (70 °C, 30 bar), PEM electrolyzer (60 °C, 30 bar) and PEM fuel cell polarization curve (60 °C and 1 bar).

of activation free energy ( $E_{a,act}$ ) are comparable with what reported in Ref. [57].

Table A3 reports main parameters related to the PEM fuel cell model. A maximum relative error on the voltage of around 2.41% was achieved by the calibration process. The reference exchange current densities ( $i_{0,ref}$ ) for the cathodic  $O_2$  reduction and anodic  $H_2$  oxidation are reported to be in the range  $10^{-9}$ – $10^{-12}$  and  $10^{-4}$ – $10^{-3}$  A/cm<sup>2</sup> [57]. The charge transfer coefficients ( $\alpha$ ) for anode and cathode are stated to be 0–1 and 0–2, respectively [57]. Our fitted values for  $i_{0,ref}$  and  $\alpha$  parameters lie within these ranges. The activation free energy values ( $E_{a,act}$ ) we found are in accordance with

what suggested by Abdin *et al.* [57]. Finally, the fitted terms referred to the membrane ionic conductivity formula ( $E_{a,mem}$  and  $\sigma_{mem,ref}$ ) provide conductivity values in line with common values for PEM fuel cells [101].

Fig. A1 shows the contributions of overpotential terms to the polarization curve for the various investigated electrochemical devices.

## References

- [1] IRENA, "Off-grid renewable energy systems: status and methodological issues," 2015.
- [2] Marocco P, et al. A study of the techno-economic feasibility of H<sub>2</sub>-based energy storage systems in remote areas. *Energy Convers Manag* 2020;211:112768.
- [3] Bin Wali S, et al. Battery storage systems integrated renewable energy sources: A bibliometric analysis towards future directions. *J Energy Storage* 2021;35: 102296.
- [4] Olabi AG, Onumaegbu C, Wilberforce T, Ramadan M, Abdelkareem MA, Al-Alami AH. "Critical review of energy storage systems". *Energy* 2021;214:118987.
- [5] G. Buffo, P. Marocco, D. Ferrero, A. Lanzini, and M. Santarelli, "Power-to-X and power-to-power routes," *Sol. Hydrog. Prod.*, pp. 529–557, 2019.
- [6] Zhang W, Maleki A, Rosen MA, Liu J. Optimization with a simulated annealing algorithm of a hybrid system for renewable energy including battery and hydrogen storage. *Energy* 2018;163:191–207.
- [7] Maleki A, Askarzadeh A. Comparative study of artificial intelligence techniques for sizing of a hydrogen-based stand-alone photovoltaic/wind hybrid system. *Int J Hydrogen Energy* 2014;39(19):9973–84.
- [8] N. D. Nordin and H. A. Rahman, "Sizing and economic analysis of stand alone photovoltaic system with hydrogen storage," *IOP Conf. Ser. Earth Environ. Sci.*, vol. 93, no. 1, 2017.
- [9] Castañeda M, Cano A, Jurado F, Sánchez H, Fernández LM. Sizing optimization, dynamic modeling and energy management strategies of a stand-alone PV/hydrogen/battery-based hybrid system. *Int J Hydrogen Energy* 2013;38(10): 3830–45.
- [10] Hosseinalizadeh R, Shakouri H, Amalnick GMS, Taghipour P. Economic sizing of a hybrid (PV-WT-FC) renewable energy system (HRES) for stand-alone usages by an optimization-simulation model: Case study of Iran. *Renew Sustain Energy Rev* 2016;54:139–50.
- [11] W. Dong, Y. Li, and J. Xiang, "Optimal sizing of a stand-alone hybrid power system based on battery/hydrogen with an improved ant colony optimization," *Energies*, vol. 9, no. 10, 2016.
- [12] F. Dawood, G. M. Shafiullah, and M. Anda, "Stand-alone microgrid with 100% renewable energy: A case study with hybrid solar pv-battery-hydrogen," *Sustain.*, vol. 12, no. 5, 2020.
- [13] Li CH, Zhu XJ, Cao GY, Sui S, Hu MR. Dynamic modeling and sizing optimization of stand-alone photovoltaic power systems using hybrid energy storage technology. *Renew Energy* 2009;34(3):815–26.
- [14] Richards BS, Conibeer GJ. A comparison of hydrogen storage technologies for solar-powered stand-alone power supplies: A photovoltaic system sizing approach. *Int J Hydrogen Energy* 2007;32(14):2712–8.
- [15] Nordin ND, Rahman HA. Comparison of optimum design, sizing, and economic analysis of standalone photovoltaic/battery without and with hydrogen production systems. *Renew Energy* 2019;141:107–23.
- [16] Gracia L, Casero P, Bourasseau C, Chabert A. Use of hydrogen in off-grid locations, a techno-economic assessment. *Energies* 2018;11(11):3141.
- [17] Perrigot A, Perier-Muzet M, Ortega P, Stitou D. Technical economic analysis of PV-driven electricity and cold cogeneration systems using particle swarm optimization algorithm. *Energy* 2020;211:119009.
- [18] Ashourian MH, Cherati SM, Mohd Zin AA, Niknam N, Mokhtar AS, Anwari M. Optimal green energy management for island resorts in Malaysia. *Renew Energy* 2013;51:36–45.
- [19] Jamshidi M, Askarzadeh A. Techno-economic analysis and size optimization of an off-grid hybrid photovoltaic, fuel cell and diesel generator system. *Sustain Cities Soc* 2019;44:310–20.
- [20] Margaret Amutha W, Rajini V. Techno-economic evaluation of various hybrid power systems for rural telecom. *Renew Sustain Energy Rev* 2015;43:553–61.
- [21] Ozden E, Tari I. PEM fuel cell degradation effects on the performance of a stand-alone solar energy system. *Int J Hydrogen Energy* 2017;42(18):13217–25.
- [22] Sinha S, Chandel SS. Review of software tools for hybrid renewable energy systems. *Renew Sustain Energy Rev* 2014;32:192–205.
- [23] Lian J, Zhang Y, Ma C, Yang Y, Chaima E. A review on recent sizing methodologies of hybrid renewable energy systems. *Energy Convers Manag* 2019; 199:112027.
- [24] Mokhtara C, Negrou B, Boufferrouk A, Yao Y, Settou N, Ramadan M. Integrated supply–demand energy management for optimal design of off-grid hybrid renewable energy systems for residential electrification in arid climates. *Energy Convers Manag* 2020;221:113192.
- [25] Dufo-López R, Bernal-Agustín JL. Multi-objective design of PV-wind-diesel-hydrogen-battery systems. *Renew Energy* 2008;33(12):2559–72.
- [26] Attemene NS, Agbli KS, Fofana S, Hissel D. Optimal sizing of a wind, fuel cell, electrolyzer, battery and supercapacitor system for off-grid applications. *Int J Hydrogen Energy* 2020;45(8):5512–25.
- [27] Maleki A, Askarzadeh A. Artificial bee swarm optimization for optimum sizing of a stand-alone PV/WT/FC hybrid system considering LPSP concept. *Sol Energy* 2014;107:227–35.
- [28] Kalinci Y, Hepbasli A, Dincer I. Techno-economic analysis of a stand-alone hybrid renewable energy system with hydrogen production and storage options. *Int J Hydrogen Energy* 2015;40(24):7652–64.
- [29] Behzadi MS, Niasati M. Comparative performance analysis of a hybrid PV/FC/battery stand-alone system using different power management strategies and sizing approaches. *Int J Hydrogen Energy* 2015;40(1):538–48.
- [30] Baghaee HR, Mirsalim M, Gharehpetian GB, Talebi HA. Reliability/cost-based multi-objective Pareto optimal design of stand-alone wind/PV/FC generation microgrid system. *Energy* 2016;115:1022–41.
- [31] Fathy A. A reliable methodology based on mine blast optimization algorithm for optimal sizing of hybrid PV-wind-FC system for remote area in Egypt. *Renew Energy* 2016;95:367–80.
- [32] Ahadi A, Liang X. A stand-alone hybrid renewable energy system assessment using cost optimization method. In: *Proceedings of the IEEE International Conference on Industrial Technology*; 2017. p. 376–81.
- [33] Li B, Roche R, Miraoui A. Microgrid sizing with combined evolutionary algorithm and MILP unit commitment. *Appl Energy* 2017;188:547–62.
- [34] Duman AC, Güler Ö. Techno-economic analysis of off-grid PV/wind/fuel cell hybrid system combinations with a comparison of regularly and seasonally occupied households. *Sustain Cities Soc* 2018;42:107–26.
- [35] Samy MM, Barakat S, Ramadan HS. A flower pollination optimization algorithm for an off-grid PV-Fuel cell hybrid renewable system. *Int J Hydrogen Energy* 2019;44(4):2141–52.
- [36] Haddidan Moghaddam MJ, Kalam A, Nowdeh SA, Ahmadi A, Babanezhad M, Saha S. Optimal sizing and energy management of stand-alone hybrid photovoltaic/wind system based on hydrogen storage considering LOEE and LOLE reliability indices using flower pollination algorithm. *Renew Energy* 2019; 135:1412–34.
- [37] Luta DN, Raji AK. Optimal sizing of hybrid fuel cell-supercapacitor storage system for off-grid renewable applications. *Energy* 2019;166:530–40.
- [38] Rullo P, Braccia L, Luppi P, Zumoffen D, Feroldi D. Integration of sizing and energy management based on economic predictive control for standalone hybrid renewable energy systems. *Renew Energy* 2019;140:436–51.
- [39] Xu C, Ke Y, Li Y, Chu H, Wu Y. Data-driven configuration optimization of an off-grid wind/PV/hydrogen system based on modified NSGA-II and CRITIC-TOPSIS. *Energy Convers Manag* 2020;215:112892.
- [40] Zhang G, Shi Y, Maleki A, Rosen MA. Optimal location and size of a grid-independent solar/hydrogen system for rural areas using an efficient heuristic approach. *Renew Energy* 2020;156:1203–14.
- [41] REMOTE project, "REMOTE project website", Online Available: <https://www.remoted-euproject.eu/> 2018 Accessed: 11-Mar-2021.
- [42] Singh A, Baredar P, Gupta B. Techno-economic feasibility analysis of hydrogen fuel cell and solar photovoltaic hybrid renewable energy system for academic research building. *Energy Convers Manag* 2017;145:398–414.
- [43] Hwang JJ, Lai LK, Wu W, Chang WR. Dynamic modeling of a photovoltaic hydrogen fuel cell hybrid system. *Int J Hydrogen Energy* 2009;34(23):9531–42.
- [44] Laoun B, Khellaf A, Naceur MW, Kannan AM. Modeling of solar photovoltaic-polymer electrolyte membrane electrolyzer direct coupling for hydrogen generation. *Int J Hydrogen Energy* 2016;41(24):10120–35.
- [45] Bakirci K. "Estimation of Solar Radiation by Using ASHRAE Clear-Sky Model in Erzurum, Turkey", *Energy Sources. Part A Recover Util Environ Eff* 2009;31(3): 208–16.
- [46] "Photovoltaic Geographical Information System (PVGIS)." [Online]. Available: <https://ec.europa.eu/jrc/en/pvgis>. [Accessed: 11-Mar-2021].
- [47] Henaou C, Agbossou K, Hammoudi M, Dubé Y, Cardenas A. Simulation tool based on a physics model and an electrical analogy for an alkaline electrolyser. *J Power Sources* 2014;250:58–67.
- [48] Marocco P, et al. Online measurements of fluoride ions in proton exchange membrane water electrolysis through ion chromatography. *J Power Sources* 2021;483:229179.
- [49] Corrêa JM, Farret FA, Canha LN, Simoes MG. An electrochemical-based fuel-cell model suitable for electrical engineering automation approach. *IEEE Trans Ind Electron* 2004;51(5):1103–12.
- [50] Ursúa A, Sanchis P. Static-dynamic modelling of the electrical behaviour of a commercial advanced alkaline water electrolyser. *Int J Hydrogen Energy* 2012;37(24):18598–614.
- [51] Balej J. Water vapour partial pressures and water activities in potassium and sodium hydroxide solutions over wide concentration and temperature ranges. *Int J Hydrogen Energy* 1985;10(4):233–43.
- [52] Hammoudi M, Henaou C, Agbossou K, Dubé Y, Doumbia ML. New multi-physics approach for modelling and design of alkaline electrolyzers. *Int J Hydrogen Energy* 2012;37(19):13895–913.
- [53] Abdin Z, Webb CJ, Gray EMA. Modelling and simulation of an alkaline electrolyser cell. *Energy* 2017;138:316–31.
- [54] Ulleberg Ø. Modeling of advanced alkaline electrolyzers: a system simulation approach. *Int J Hydrogen Energy* 2003;28:21–33.
- [55] V. Liso, G. Savoia, S. S. Araya, G. Cinti, and S. K. Kær, "Modelling and Experimental Analysis of a Polymer Electrolyte Membrane Water Electrolysis Cell at Different Operating Temperatures," *Energies*, vol. 11, no. 12, 2018.

- [56] G. Tsotridis and A. Pilenga, "EU harmonized terminology for low-temperature water electrolysis for energy-storage applications," 2018.
- [57] Abdin Z, Webb CJ, Gray EMA. PEM fuel cell model and simulation in Matlab-Simulink based on physical parameters. *Energy* 2016;116:1131–44.
- [58] Espinosa-López M, et al. Modelling and experimental validation of a 46 kW PEM high pressure water electrolyzer. *Renew Energy* 2018;119:160–73.
- [59] García-Valverde R, Espinosa N, Urbina A. Simple PEM water electrolyser model and experimental validation. *Int J Hydrogen Energy* 2012;37(2):1927–38.
- [60] Rahim AHA, Tijani AS, Shukri FH, Hanapi S, Sainan KI. Mathematical modelling and simulation analysis of PEM electrolyzer system for hydrogen production. 3rd IET Int Conf Clean Energy Technol 2014:1–7.
- [61] Colbertaino P, Gómez Aláez SL, Campanari S. Zero-dimensional dynamic modeling of PEM electrolyzers. *Energy Procedia* 2017;142:1468–73.
- [62] Schalenbach M, Carmo M, Fritz DL, Mergel J, Stolten D. Pressurized PEM water electrolysis: Efficiency and gas crossover. *Int J Hydrogen Energy* 2013;38(35):14921–33.
- [63] Trinke P, Haug P, Brauns J, Bensmann B, Hanke-Rauschenbach R, Turek T. Hydrogen Crossover in PEM and Alkaline Water Electrolysis: Mechanisms, Direct Comparison and Mitigation Strategies. *J Electrochem Soc* 2018;165(7):F502–13.
- [64] Saleh IMM, Ali R, Zhang H. Simplified mathematical model of proton exchange membrane fuel cell based on horizon fuel cell stack. *J Mod Power Syst Clean Energy* 2016;4(4):668–79.
- [65] Park SK, Choe SY. Dynamic modeling and analysis of a 20-cell PEM fuel cell stack considering temperature and two-phase effects. *J Power Sources* 2008;179(2):660–72.
- [66] Amphlett JC, Baumert RM, Mann RF, Peppley BA, Roberge PR, Harris TJ. Performance modeling of the Ballard Mark IV solid polymer electrolyte fuel cell: I. mechanistic model development. *J Electrochem Soc* 1995;142:1–8.
- [67] Parra D, Patel MK. Techno-economic implications of the electrolyser technology and size for power-to-gas systems. *Int J Hydrogen Energy* 2016;41(6):3748–61.
- [68] Buttler A, Spliethoff H. Current status of water electrolysis for energy storage, grid balancing and sector coupling via power-to-gas and power-to-liquids: A review. *Renew Sustain Energy Rev* 2018;82:2440–54.
- [69] Mayyas A, Ruth M, Pivovar B, Bender G, Wipke K. "Manufacturing cost analysis for proton exchange membrane water. Electrolyzers" 2019.
- [70] Büchi FN, et al. Towards re-electrification of hydrogen obtained from the power-to-gas process by highly efficient H<sub>2</sub>/O<sub>2</sub> polymer electrolyte fuel cells. *RSC Adv* 2014;4(99):56139–46.
- [71] Tractebel and Hinicio, "Study on early business cases for H<sub>2</sub> in energy storage and more broadly power to H<sub>2</sub> applications," 2017.
- [72] A. Mayyas and M. Mann, "Manufacturing competitiveness analysis for hydrogen refueling stations and electrolyzers," 2018. [Online]. Available: [https://www.hydrogen.energy.gov/pdfs/review18/mn017\\_mann\\_2018\\_p.pdf](https://www.hydrogen.energy.gov/pdfs/review18/mn017_mann_2018_p.pdf). [Accessed: 31-Oct-2020].
- [73] Godula-Jopek A, Stolten D. *Hydrogen production by electrolysis*. Wiley-VCH; 2015.
- [74] P. Marocco, D. Ferrero, M. Gandiglio, and M. Santarelli, "Deliverable number 2.2 Technical specification of the technological demonstrators," 2018.
- [75] LG. "LG NeON® R solar module." [Online]. Available: <https://www.lg.com/us/business/solar-panels/lg-LG365Q1C-A5>. [Accessed: 11-Mar-2021].
- [76] Schopfer S, Tiefenbeck V, Staake T. Economic assessment of photovoltaic battery systems based on household load profiles. *Appl Energy* 2018;223:229–48.
- [77] I. Tsiropoulos, D. Tarvydas, and N. Lebedeva, "Li-ion batteries for mobility and stationary storage applications," 2018.
- [78] Zia MF, Elbouchikhi E, Benbouzid M. Optimal operational planning of scalable DC microgrid with demand response, islanding, and battery degradation cost considerations. *Appl Energy* 2019;237:695–707.
- [79] Federal Ministry for Economic Affairs and Energy, "Markets for Battery Storage. Sub-sector analysis on the market potential for battery storage in Tanzania," 2015.
- [80] Moretti L, Astolfi M, Vergara C, Macchi E, Pérez-Arriaga JI, Manzolini G. A design and dispatch optimization algorithm based on mixed integer linear programming for rural electrification. *Appl Energy* 2019;233–234:1104–21.
- [81] Bordin C, Anuta HO, Crossland A, Gutierrez IL, Dent CJ, Vigo D. A linear programming approach for battery degradation analysis and optimization in off-grid power systems with solar energy integration. *Renew Energy* 2017;101:417–30.
- [82] Proost J. State-of-the art CAPEX data for water electrolyzers, and their impact on renewable hydrogen price settings. *Int J Hydrogen Energy* 2019;44(9):4406–13.
- [83] M. Santos and I. Marino, "Energy analysis of the Raggovidda integrated system," 2019.
- [84] Shehzad MF, Abdelghany MB, Liuzza D, Mariani V, Glielmo L. Mixed logic dynamic models for MPC control of wind farm hydrogen-based storage systems. *Inventions* 2019;4(4):1–17.
- [85] Thomas D, Mertens D, Meeus M, Van der Laak W, Francois I. *Power-to-gas Roadmap for Flanders*. Brussels 2016.
- [86] J. Brauns and T. Turek, "Alkaline water electrolysis powered by renewable energy: A review," *Processes*, vol. 8, no. 2, 2020.
- [87] Battelle Memorial Institute, "Manufacturing Cost Analysis of PEM Fuel Cell Systems for 5- and 10-kW Backup Power Applications," 2016.
- [88] Torreglosa JP, García-Triviño P, Fernández-Ramírez LM, Jurado F. Control based on techno-economic optimization of renewable hybrid energy system for stand-alone applications. *Expert Syst Appl* 2016;51:59–75.
- [89] Battelle Memorial Institute, "Manufacturing Cost Analysis: 1, 5, 10 and 25 kW Fuel Cell Systems for Primary Power and Combined Heat and Power Applications," 2017.
- [90] Few S, Schmidt O, Gambhir A, Stephenson E, DelCore A. "Energy storage trends for off-grid services in emerging markets. Insight from Social Enterprises" 2018.
- [91] Gabrielli P, Gazzani M, Mazzotti M. Electrochemical conversion technologies for optimal design of decentralized multi-energy systems: Modeling framework and technology assessment. *Appl Energy* 2018;221(April):557–75.
- [92] El-Kharouf A, Chandan A, Hattenberger M, Pollet BG. Proton exchange membrane fuel cell degradation and testing: Review. *J Energy Inst* 2012;85(4):188–200.
- [93] Jakhriani AQ, Rigit ARH, Othman AK, Samo SR, Kamboh SA. Estimation of carbon footprints from diesel generator emissions. In: *Proceedings of the 2012 International Conference in Green and Ubiquitous Technology*; 2012, 2012., p. 78–81.
- [94] Wendt H, Plzak V. Electrocatalytic and thermal activation of anodic oxygen and cathodic hydrogen-evolution in alkaline water electrolysis. *Electrochim Acta* 1983;28(1):27–34.
- [95] Stojadinovic J, et al. Electrochemical characterization of porous diaphragms in development for gas separation. *ECS Electrochem Lett* 2012;1(4):F25–8.
- [96] Abdin Z, Webb CJ, Gray EM. Modelling and simulation of a proton exchange membrane (PEM) electrolyser cell. *Int J Hydrogen Energy* 2015;40(39):13243–57.
- [97] Carmo M, Fritz DL, Mergel J, Stolten D. A comprehensive review on PEM water electrolysis. *Int J Hydrogen Energy* 2013;38(12):4901–34.
- [98] Yigit T, Selamet OF. Mathematical modeling and dynamic Simulink simulation of high-pressure PEM electrolyzer system. *Int J Hydrogen Energy* 2016;41(32):13901–14.
- [99] Springer TE, Zawodzinski Ta, Gottesfeld S. Polymer electrolyte fuel cell model. *J Electrochem Soc* 1991;138(8):2334–42.
- [100] Bessarabov D, Wang H, Li H, Zhao N. *PEM Electrolysis for Hydrogen Production: Principles and Applications* 2015.
- [101] O'Hayre R, Cha S-W, Colella WG, Prinz FB. *Fuel cell fundamentals*. Third Edit: Wiley; 2016.